Comparison of Multiple Degrees of Electrode Surface Roughness: Impedance, Charge Storage Capacity, Biofouling and Biocompatibility

Mungo Arthur Elms

Submitted in accordance with the requirements for the degree

of Masters of Science by Research

The University of Leeds

Faculty of Biological Sciences

School of Biomedical Sciences

February 2017

Supervisor: Dr. Samit Chakrabarty

Co-Supervisor: Dr. D Paul Steenson

The candidate confirms that the work submitted is his own and that appropriate credit has been given where reference has been made to the work of others.

i. Acknowledgements

I would like to dedicate this thesis to my parents, Charles and Fenella Elms. They have always been there with unquestioning support, love and care. I owe my academic career to them. I cannot convey how thankful I am for your help.

I would like to thank my supervisors, Samit Chakrabarty and Paul Steenson. Paul's wealth of technical knowledge has been invaluable. Samit's enthusiasm, good humour and willingness to take a chance on me as an undergraduate is what brought me to do a masters in the first place. I am also thankful for Samit's unwavering commitment to eliminating 'Mungoisms' from my writing, it has helped immensely.

To everyone in the 5.55 seating area, I will always be thankful for the laughs, I only hope you can now find someone else to satiate Sian's tea consumption.

To my mentor and friend Andrew Tsatsanis, your teaching has been both terrifying and deeply enjoyable. It has made all of the cell culture work possible and my masters even more enjoyable. I will never look at pipettes the same way again.

This research has been carried out by a team which has included Chris Russell. My own contributions, fully and explicitly indicated in the thesis, have been outlined in sections 2.4 – 2.8. Chris' contributions have been outlined in sections 2.1 – 2.3. Without Chris' help and technical knowledge, this project would have not have existed in this form. He has worked tirelessly on this project and I am very extremely grateful.

Finally, to my girlfriend Meera. Your kindness, love and inspiration throughout this experience has kept me grounded and happy. Without failure, you have made the hard times much easier and the good times so much better. Thank you.

ii. Abbreviations

AC – Alternating Current

aCSF – Artificial Cerebral Spinal Fluid

AFM – Atomic Force Microscopy

Au - Gold

BSA – Bovine Serum Albumin

CSC – Charge Storage Capacity

CSCa – Anodic Charge Storage Capacity

CSCc – Cathodic Charge Storage Capacity

CSF – Cerebral Spinal Fluid

CV – Cyclic Voltammetry

DAPI - 4',6-diamidino-2-phenylindole

DC – Direct Current

ECM – Extracellular Matrix

HSA – Human Serum Albumin

IgG – Immunoglobulin G

NG2 – Neural/glial antigen 2

PBS – Phosphate Buffer Saline

PBST – PBS containing Triton

Ra – Average Roughness

RIE – Reactive Ion Etching

Rms – Root Mean Square Roughness

SD – Standard Deviation

SEM – Standard Error of the Mean

iii. Abstract

Devices called neural electrodes are generally used to record and / or stimulate neural activity whilst extracellularly interfacing with neurons. The ultimate goal of the field is to develop neural electrodes that can continuously record and / or stimulate neural activity for long periods of time (10+ years). Electrodes require low electrode impedance to enable good signal to noise ratio and a high capacity for chemically stable injection of charge (CSC) for stimulating neural activity. Electrode function typically deteriorates after a few months *in-vivo* due two factors: biofouling and local cellular response (glial scarring). Biofouling is theorised to be an accumulation of multiple proteins at the electrode surface. However this has only been backed up experimentally by single protein models in literature. Electrodes need to be able to combat the effects of biofouling and glial scarring. This study uses nanometre scale roughened gold (Au) electrodes. Electrode roughening has previously been shown to lower impedance, increase CSC and reduce glial response and the effects of biofouling. We compared multiple degrees of roughness with the aim of finding the optimal degree for improving impedance, CSC, biofouling and cellular response. We found that surface roughening increased impedance and only increased CSC for two only degrees of roughness. To find the optimal degree of roughness across conditions, we suspect a larger range of roughness may be necessary to lower impedance with our fabrication technique. This study is the first to use a multiprotein biofouling model. Contrary to literature, we found that incubation with protein decreased impedance, likely due to protein-protein interactions not accounted for in single protein models. Biocompatibility was improved for two degrees of Au roughness. Roughening of SU8, a polymer used to surround the electrodes, decreased biocompatibility. We also used artificial cerebral spinal fluid (aCSF) as an electrolyte, which is more chemically similar to *in-vivo* than commonly used phosphate buffered saline solution (PBS). The use aCSF as a medium was significant as the measures in aCSF were different from that in PBS.

iv. Table of Contents

v. Table of Figures

Chapter 1: Introduction

Neural probes are devices commonly used to extracellularly interface with neurons where they record and/or stimulate neuronal activity in the brain and spinal cord. They are typically multi-layered devices, with the interfacing layer consisting of electrically conductive regions (electrodes) made from an electrically conductive material. This is surrounded by an electrically insulating material, or 'passivation' material. Electrodes are used to restore sensory-motor function to patients with neurological disorders. For this to be clinically viable, they must be able to provide stable, high quality recordings of neuronal activity for 10 years. Stimulating electrodes must also be able to inject sufficient charge across the electrode-tissue interface to cause depolarisation of surrounding neuronal membranes. Unfortunately, electrode recording and stimulation performance currently deteriorates after a few months. This is due to two problems.

(1) Impedance increase from biofouling. Neuronal activity can be recorded either as voltage changes in the surrounding field of charge (local field potential) or as sharp voltage changes (spikes) which are caused by the membrane depolarisation of individual neurons. Increases in the electrical impedance at the electrode-tissue interface can decrease sensitivity, potentially leading to the failure to record either of these. Inserting a probe into neural tissue results in the rupturing of blood vessels and cell lysis (Kozai et al. 2010; Bjornsson et al. 2006). Proteins released in this process, as well as those already in the extracellular space, adhere to the surface of the electrode in a process termed biofouling (Malaga et al. 2016; Sommakia et al. 2009; Sommakia et al. 2014). Biofouling increases impedance, thus decreasing recording sensitivity (Moulton et al. 2003; Ying et al. 2004; Newbold et al. 2010). An aim of this study was therefore to reduce impedance increase following biofouling.

(2) Cellular response to probe. The tissue damage caused by probe insertion initiates the activation of nearby glial cells (astrocytes and microglia). These migrate to the surface of the probe, forming a sheath of protective tissue around it (Kozai et al. 2014). This tissue is known as glial scarring and is thought to increase impedance due to an increased solution

resistance through the scaring tissue (Roitbak & Syková 1999). Scar formation through the infiltration of glial cells also increases the distance between the probe and the nearest neurons. This is because activated glial cells found in the scar produce proteoglycans (such as NG2, dermatan and keratin sulphate) which block neurite extension (Smith-Thomas et al. 1995; Elizabeth M. Powell et al. 1997). Furthermore, probe insertion causes inflammatory response associated with local neuronal degeneration (McConnell et al. 2009; Biran et al. 2005). This response has been shown to be regulated by activated glial cells, implying greater amounts of glial scarring results in greater amounts of neuronal degeneration (Babcock et al. 2003; Sakurai-Yamashita et al. 2006). Combined, these factors increase probe-neuron distance. This decreases recording sensitivity as an increased distance results in greater charge dispersal. An aim of this study is therefore to reduce glial scar formation around the probe. A probe's ability to reduce glial scar formation is referred to as biocompatibility.

Recent strategies to bypass these problems include coating the electrode with materials that provide a 'rough' (i.e. less planar) electrode surface such as the conducting polymers Poly(3,4-ethylenedioxythiophene) (PEDOT) or polypyrrole, titanium nitride or sputtered iridium oxide films (SIROF) (Cellot et al. 2016; Venkatraman et al. 2009; Castagnola et al. 2015; Meijs et al. 2016; Kim et al. 2009; Chen et al. 2011). Rough surfaces allow for increased electrode surface area whilst maintaining a small electrode (and thus probe) size. This is advantageous because large electrode surface area decreases impedance (Koklu et al. 2016), as well as increases the amount of charge that can be injected into the tissue (Bhandari et al. 2011; Aurian-Blajeni et al. 1987). The logic is that by decreasing electrode impedance initially, the effects of biofouling will not be so damaging to electrode function (Kozai et al. 2016). A smaller probe will also cause less tissue damage, and so reduce the amount of glial cell activation (Patel et al. 2015; Kozai et al. 2012). An alternative strategy to provide a rough electrode surface is to roughen the electrode material.

This study uses nanometre scale roughened Au electrodes. Roughened electrodes may provide a more stable alternative than conducting polymers which are prone to delamination and are considerably cheaper to produce than SIROF (Cui et al. 2003; Boehler et al. 2015). Roughening has been shown to lower impedance of gold (Au) electrodes by up to 98% (Seker et al. 2010; Chung, et al. 2015). Roughening Au also increases charge storage capacity (CSC), which is a measure of how much charge can be passed between the electrode surface and the tissue (Bhandari et al. 2011). Moreover, Patel et al., (2013) found that a degree of roughness on the nanometre scale had a smaller increase in impedance following fibrinogen adsorption in comparison to micrometre scale roughness or planar. This suggests surface roughening may reduce the effects of biofouling. However, different proteins bind with different affinities (Williams et al. 1985; Michel et al. 2008) and effect impedance to different extents (Moulton et al. 2004). Therefore, a more accurate model of biofouling would require a mixture of proteins similar to those released following probe insertion. For this reason, a multiprotein model was used in this study.

Another advantage of roughening is the ability to regulate the degree of roughness in fabrication. Greater degrees of surface roughening have lower impedance and higher CSC compared to lower degrees (Chung, et al. 2015). However to our knowledge, no one has tested impedance and CSC for multiple degrees of roughness. One of the aims of this study was therefore to find which degree of roughness had the lowest impedance and highest CSC. The hypothesis was that higher degrees of roughness would have lower impedance and higher CSC.

Greater amounts of fibronectin have been shown to bind to higher degrees of roughness (Salakhutdinov et al. 2008). It therefore seems likely that there will be greater amounts of non-specific protein adsorption on rougher surfaces. For this reason it is hypothesized that there will be a larger impedance increase from biofouling with higher degrees of roughening. It is also hypothesized that greater degrees of roughness will have lower impedance before biofouling. Since the aim is to lower impedance increase following biofouling, one of the

objectives of this study is to find an optimal degree of roughness with the lowest impedance following protein adhesion.

As reviewed by Biggs et al. (2010), there is a large amount of literature demonstrating cell sensitivity to nanometre scale surface features. *In-vivo*, cells bind to the extracellular matrix (ECM) which has been shown to have nanometre scale features (Bosman & Stamenkovic 2003). Nanometre scale roughening is therefore of interest as it may reproduce the *in-vivo* environment. In line with this, studies have also demonstrated how *in-vitro* biocompatibility is increased with nano-roughened Au in comparison to smooth controls (Chapman et al. 2015; 2016). Kurtulus and Seker (2012) showed that whilst astrocytic cell density did not change with increased degrees of roughness, cell size did implying greater amounts of focal adhesions to the Au surface. However, they stated that a wider range of degrees of roughness was necessary to find the optimal degree of roughness. This study has used a wide range of roughness in an attempt to find an optimal degree. To our knowledge, no studies have looked at the effect of roughening passivation layer materials on biocompatibility. The passivation layer covers the vast majority of the probe surface. The biocompatibility of the passivation layer is therefore a substantial factor in the biocompatibility of the probe. For these reasons, this study compared the biocompatibility of multiple degrees of roughness of both an electrode and passivation material. It is hypothesized that rougher surfaces will have greater biocompatibility.

1.1 Aims and Objectives

The aim was to find the single or range of optimal degrees of roughness for lowering impedance *and* increasing charge storage capacity, as well as decreasing the effects of both biofouling and glial scarring.

Objectives:

- Find the degree of roughness with the lowest impedance.
- Find the degree of roughness with the highest charge storage capacity.

- Find the degree of roughness with the smallest impedance increase from biofouling.
- Find the degree of roughness with the most favourable response from glial cells (i.e. high density of non-activated astrocytes and low density of activate astrocytes).
- Find the degree or range of degrees with an overlap in the above.

1.2 Probe Materials and Design Background

Au was used as an electrode material in this study. As mentioned, the aim of this study was to find the range and/or degree of roughness that was optimal consistently with tests (i.e. impedance, CSC, biofouling and biocompatibility). Roughened Au and platinum both function well as electrode materials (Cogan 2008). However, platinum faces drawbacks such as poor durability and increased difficulties in fabrication (Desai et al. 2010). Au is advantageous because roughening appears to improve function in multiple conditions across studies. For example, roughening has consistently lowered impedance and increased CSC (Koklu et al. 2016; Hu et al. 2006; Chung, et al. 2015), as well as improved biocompatibility (Hai et al. 2009; Seker et al. 2010). It was for this reason we thought Au would be the most suitable material for this study.

SU8 was used as a passivation layer in this study. As outlined by Barrese et al. (2013), passivation materials can cause electrode failure in two ways: poor biocompatibility and delamination. SU8 has been used extensively for microprobes designed for both microfluidic drug delivery and neural recording due to excellent biocompatibility (Altuna et al. 2012; 2013; 2015). SU8 also has less of a tendency to delaminate than the commonly used polyimide (Prasad et al. 2012). It is for these two reasons we chose to use SU8 in this study.

This study was designed as a pilot study to test our roughened electrode technologies potential to function *in-vivo*. For this reason, we chose to use an electrode design similar to one used *in-vivo.* The mask used for electrode fabrication was designed in a previous MSc project for this purpose.

Chapter 2: Literature Review

2.1 A Brief Overview of Capacitance and Electrical Impedance

In this study we compared the electrical impedance of several degrees of roughness. Electrical impedance is a measure of resistance to the flow of charge in an AC (alternating current) circuit. In this study, the current flowed between two electrodes submerged in an electrolyte. Impedance is comprised of two parts, the 'real' and the 'imaginary'. The real is electrical resistance and is also comprised of two parts: First, diffusion resistance occurring as charged particles (in this case solvated ions) flow towards/away from the electrode surface through the electrolyte solution. The second is the resistance to the flow of charge across the electrode – electrolyte interface, known as charge transfer resistance. Increase in either type of resistance equals *increased* impedance. The imaginary part is comprised of either capacitance or inductance at the electrode-electrolyte interface. Inductance is phenomena whereby current is forced through a conductor by a magnetic field surrounding it. However, the inductance of the electrode from the charge in the bulk of the solution is generally considered negligible in electrochemical measurements like these. This is because it is overshadowed by the comparatively higher charge density contributing to capacitance

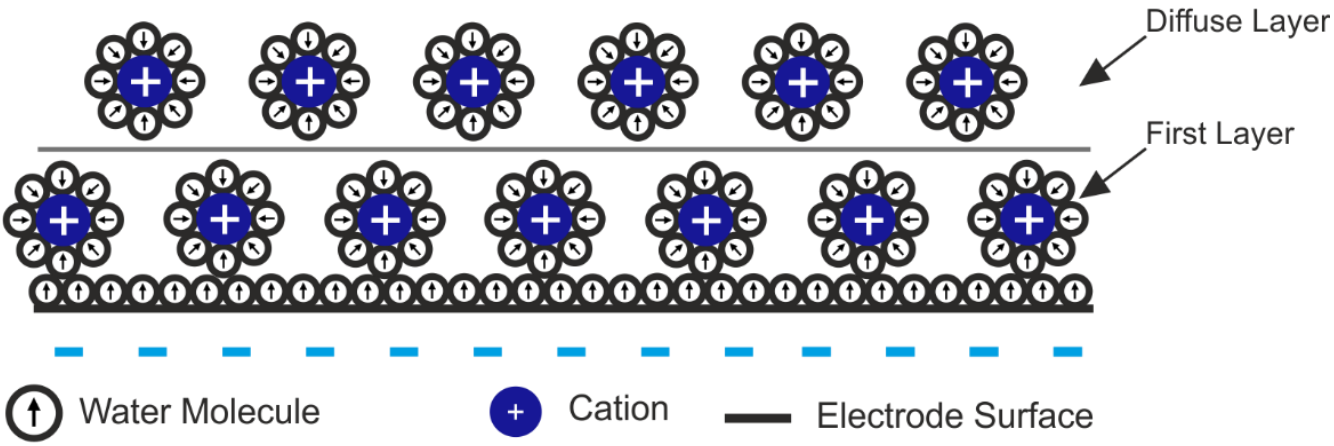

Figure 1 Schematic representation of the electrochemical double layer. The first layer is formed by polarised water molecules aligned with the electrode surface and ions accumulated at the electrode surface. In this example the electrode is negatively charged. The second layer is a diffuse layer, but it generally screens ions in the bulk of the solution.

(Alexander & Sadiku 2001). Capacitance is formed by a build-up of charge at the electrode surface through the accumulation of solvated ions, oppositely charged to the electrode (figure 1). Increased capacitance equals *decreased* impedance. Capacitance at the electrode surface forms a double layer, with the first layer consisting of ions tightly packed against the electrode surface and a second more loosely distributed layer. Ions of opposite charges are able to diffuse through the second layer, but are generally screened by the charge attracted to the electrode (figure 1). As capacitance occurs at the electrode surface, a larger surface area should result in a greater capacitance, thereby lowering impedance. As roughening increases electrode surface area, it is expected to raise capacitance and thus lower the impedance. This is why roughening electrodes typically lowers impedance.

2.2 A Brief Overview of Charge Injection

In this study we compared the amount of charge each degree of roughness is capable of storing at its surface for charge injection (CSC). Charge passage across the electrode-electrolyte inteface, or charge injection, involves the transfer of electron flow in the

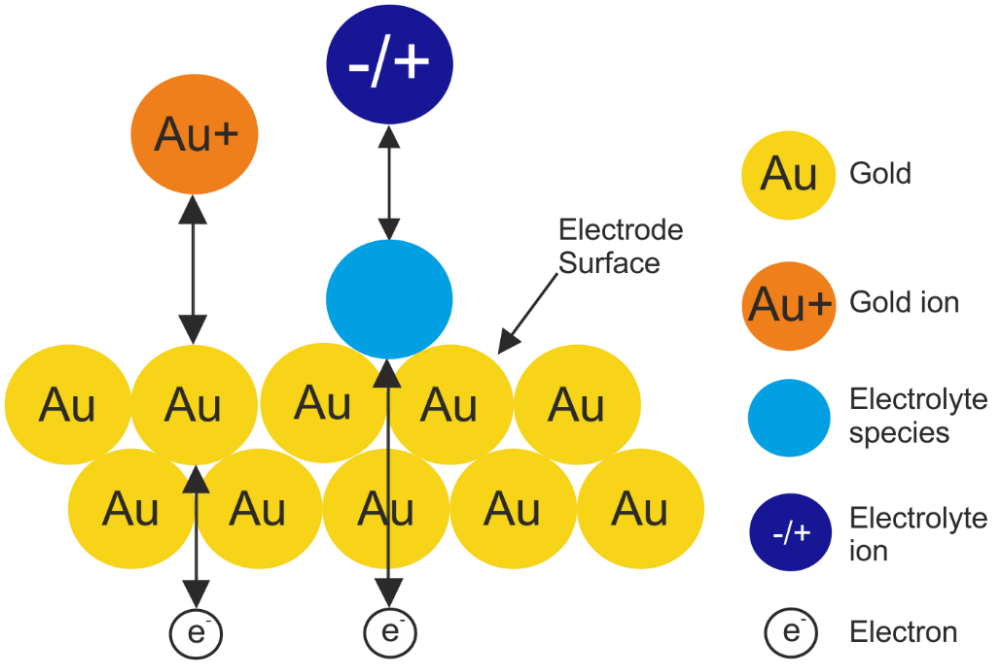

Figure 2 Faradaic charge injection mechanism. Charge is passed between the electrode and electrolyte by ions leaving / adhering to the electrode surface. Electrons flow through the electrode towards/away surface molecules which undergo reduction/oxidation reactions.

electrodes to ion flow in the electrolyte by two mechanisms: capacitive and faradaic. As described above (section 2.1), capacitance is formed by the charging and discharging of the electrochemical double layer at the electrode surface (Frumkin 1960) (figure 1, section 2.1). Faradaic reactions are reduction/oxidation (redox) reactions which involve the transfer of electrons across the electrode-electrolyte interface (figure 2). Faradaic reactions require species found either on the surface of the electrode or in solution to undergo redox reactions at the electrode surface (Cogan 2008). Faradaic reactions are often confined to a surface monolayer which results in a charge build up at the electrode-electrolyte interface (similar to capacitance), known as pseudocapacticance. As both capacitive and faradaic reactions take place at the electrode surface, a greater electrode surface area should result in a greater flow of charge (Aurian-Blajeni et al. 1987). For this reason, rough surfaces are expected to have a larger amount of charge flowing to/through the electrode-electrolyte interface than planar surfaces. This is why roughening electrodes typically increases the electrodes CSC.

2.3 An Overview of the Role of Activated vs Non Activated Astrocytesin Electrode Failure

In this study we compared the biocompatibility of several degrees of roughness using activated and non-activated astrocytes (a type of glial cell). Non-activated astrocytes are found ubiquitously in all non-developmental, undamaged neural tissue in the central nervous system (Volterra & Meldolesi 2009). They are considered to be ‘helper’ cells by facilitating neuronal survival and development (Walsh et al. 1992).

An increased neuron-electrode distance decreases recording sensitivity since charge flowing between the two is dispersed over distance. To form connections with each other, neurons extend process called neurites. This process is facilitated by non-activated astrocytes (Walsh et al. 1992). Non-activated astrocytes at the probe surface may therefore decrease neuron-electrode distance by increasing the amount of neurite extension around the probe, thus improving recording sensitivity. It is for this reason one objective of the study was to find the degree of roughness most favourable to non-activated astrocytes.

We chose activated astrocytes in this study because, unlike non-activated astrocytes, they increase neuron-electrode distance. Activated astrocytes are found in the central nervous system during development and in the event of tissue damage (Powell et al. 1997 a). Tissue damage caused during probe insertion results in the activation of nearby astrocytes which migrate to the probe surface (Szarowski et al. 2003; Biran et al. 2005). Once there, they form a key component of glial scaring tissue (Buffo et al. 2010). The addition of astrocytes thickens the glial scarring tissue, thus increasing the neuron-probe distance. In addition, activated astrocytes differ from non-activated because they produce proteoglycans such as dermatan and keratin sulphate and NG2 (neural/glial antigen) which block neurite extension (Smith-Thomas et al. 1995; Powell et al. 1997). The combination of these two effects is to increase electrode-neuron distance, thus reducing electrode recording sensitivity. It is for this reason one objective of this study was to find the degree of roughness least favourable to activated astrocytes.

2.4 Overview of Cell Binding Process and the Effects of Roughness

In this study we measured the cell density of activated and non-activated astrocytes adhered to roughened surfaces in order to compare biocompatibility. As mentioned, glial cells migrate and adhere to the surface of the inserted probe during glial scar formation (Szarowski et al. 2003; Kozai et al. 2012). Cell adhesion is affected by surface roughness. To understand how roughness affects this, the mechanisms of cell adhesion will now be discussed.

When cells bind to material surfaces, they adhere to a protein layer adsorbed within minutes of coming into contact with tissue (Diener et al. 2005; Triplett & Pavalko 2006). This occurs through activation of α and β-chain transmembrane proteins known as integrins (Cohen et al. 2004). Integrins bind specifically to proteins found in the extracellular matrix such as fibronectin, vitronectin and laminin (García 2005). Intracellularly, integrins form supramolecular complexes that contain structurally adaptive proteins such as vinculin, talin and paxillin, as shown in figure 3 (Burridge 1988; Bershadsky et al. 2006). Integrin binding to these proteins alters integrin confirmation and clustering. Increased integrin clustering leads

to the formation of focal anchoring complexes between the cell and the material surface which are reinforced intracellularly with F-actin and α-actinin filaments (Biggs et al. 2010). As in figure 3, intracellular adhesion plaques are formed as a greater amount of integrins are recruited to the adhesion complex. As the size of the adhesion plaque increases with integrin recruitment, the adhesion strength between the cell and surface also increases (Ward & Hammer 1993; Balaban et al. 2001). The formation of adhesion plaques of a sufficient size is therefore essential in providing the cell with the force required for anchorage.

Surface morphology has a large effect on the success of this process. Integrin interactions with nanometre scale features are sensitive to both spacing and the x, y, z dimensions of the surface features (Curtis et al. 2001). Generally speaking, if the size of surface protrusions and pits are too small or deep, integrin binding is limited. For example, the force required to detach fibroblasts bound to roughened Au surfaces was decreased if the distance between integrin molecules was 70 - 300 nm (Selhuber-Unkel et al. 2008). It was believed that spacing greater than 60 - 70 nm disrupts protein recruitment to the adhesion plaque. However if surface protrusions are large and shallow enough, integrin recruitment is

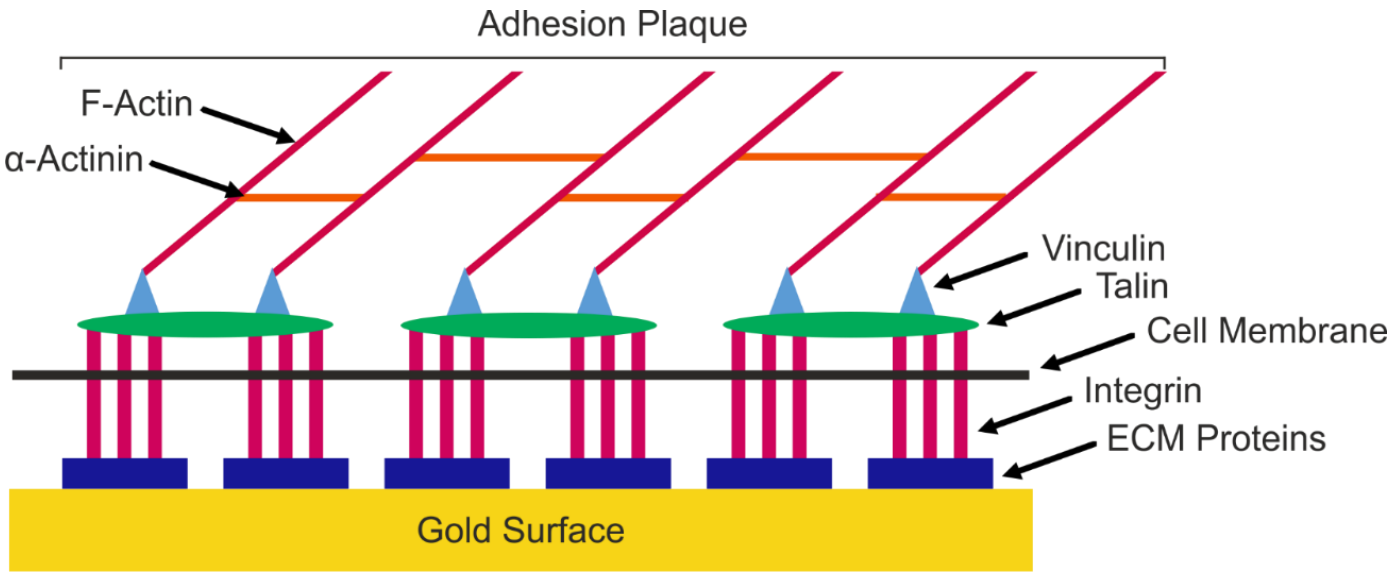

Figure 3 Schematic diagram of the focal anchoring complexes connecting to an intracellular adhesion plaque. Transmembrane integrins bind extracellular matrix (ECM) proteins extracellularly. Intracellularly, integrins form supramolecular complexes containing vinculin and talin which bind to actin. These accumulate as more integrins are recruited, forming plaques.

increased (Lim et al. 2005). Biggs et al. (2010) argue protrusions with a height and spacing > 70 nm, and widths < 70 nm are disruptive to cell binding, whilst protrusions with the opposite dimensions aid binding by providing tactile stimuli for growth.

Chapter 3: Materials & Methods

3.1 Materials

For all electrode measurements either 1 x phosphate buffer saline (PBS) (VWR™) or 1 x artificial cerebral spinal fluid (aCSF) (as in table 1) were used as electrolyte. The ingredients of the RIPA (Radioimmunoprecipitation assay) buffer (Pierce®) used in sections 3.5 and 3.6.1 are also given in table 1.

3.2 Fabrication

3.2.1 Fabrication Materials

The glass coverslip was purchased from Sigma®. The SU-8 used was the 2002 Microposit™ formulation and was purchased from the Microposit™ website. The S1813 photoresist was also manufactured by Microposit™. The reactive ion etching (RIE) machine was manufactured by JLS designs™.

3.2.2 Roughened and non-Roughened Electrode Fabrication Process

Roughened and non-roughened electrodes for *in-vitro* analysis were fabricated. Figure 4 is a schematic of the process. A 25 x 25 x 0.2 mm glass Corning cover slip was used as a host substrate for the whole process. Onto this, a 2-µm-thick layer of SU8 was spun, exposed and cured, as per manufacturer guidelines (figure 4 A). A 1 µm thick layer of S1813 photoresist was used to define a 9 contact array of 20-µm-diameter disks that were photo-lithographically defined. Each disk had an undercut profile which allowed for a clean lift off for the metal following deposition (figure 4 B). The mask was originally designed for a probe intended to penetrate tissue (figure 5). The undercut profile was defined using a chlorobenzene chemical treatment of S1813 prior to development in MF319 (figure 4 C). The SU8 was then micro-roughened using RIE (figure 4 D). This was not done for the non-

Table 1 Ingredients for the materials used in sections 3.4,35 and 3.6. PBS was purchased in tablet form. The ingredients for RIPA and aCSF were purchased separately from the same supplier. All three were made using de-ionised water.

Material	**Ingredients and Concentration (mM)**							**pH**	**Supplier**
Phosphate Buffer Saline (PBS)	NaCl	KCl	Na_2HPO_4	KH_2PO_4				7.25	VWR®
	137	2.7	10	1.8					
Artificial Cerebral Spinal Fluid (aCSF)	NaCl	KCl	KH_2PO_4	$NaHCO_3$	$MgSo_4.7H_2O$	d-glucose	$CaCl_2.2H_2O$	7.83	Pierce®
Homemade	125	3	1.25	25	1.25	10	2.5		
Radioimmunoprecipitation Assay Buffer (RIPA) Homemade	NaCl 150	Tris•HCl 25	1% (w/v) sodium deoxycholate	1% (w/v) nonyl phenoxypolyethoxylethanol	0.1% (w/v) sodium dodecyl sulphate			8.08	Pierce®

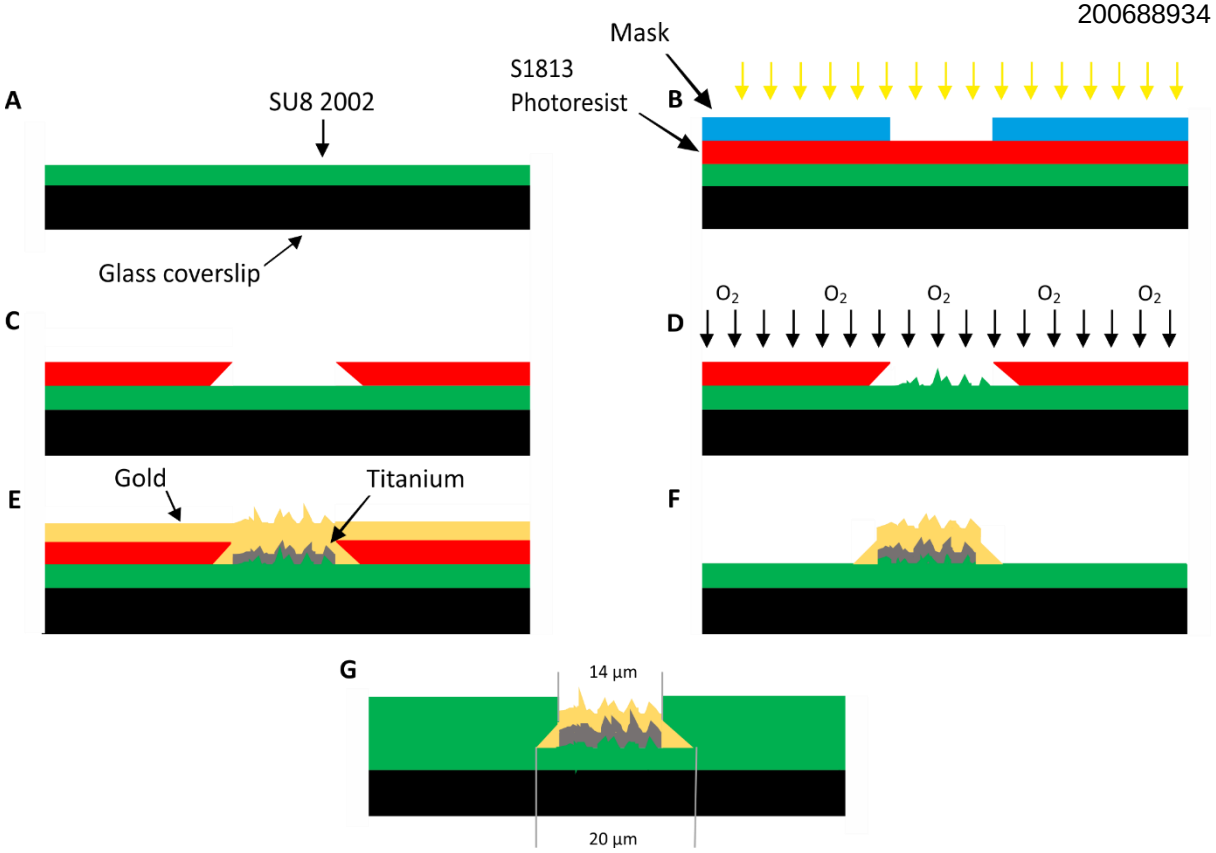

Figure 4 Simplified schematic diagram outlining the roughened electrode array fabrication process. A 2 µm thick layer SU8 2002 was spun and cured on a glass coverslip. B S1813 photoresist used to define 9 electrode array. C Chlorobenzene treatment creates undercut. D Defined array was roughened with reactive ion etching. E Titanium and then gold was deposited. F S1813 removed G Photo-patterned SU8 passivation layer. Step D was skipped for non-roughened electrodes.

roughened controls. RIE uses a chemically reactive plasma (O_2, 25 sccm at 30 m Torr) to remove material deposited on a surface. It does this using an electromagnetic field applied to the surface at a radio frequency (13.56 MHz), with a direct current bias that results in a net plasma ion flow towards the surface. The radiofrequency power value determines the selected roughness. For this reason, degrees of roughness are given in values of power (0 – 300 W). Since the non-roughened controls did not undergo this step, their power value is 0 W.

After SU8 roughening, a 10-nm-thick adhesion layer of titanium metal was deposited, followed by a 100-nm-thick layer of contact metal (figure 4 E). Here we have used gold (Au). The S1813 was removed with acetone to reveal the electrical contact pattern (figure 4 F). The electrical interconnects were then passivated using a photo-patterned 1-µm-thick layer of SU8, leaving 14-µm-diameter electrical contacts (referred to as electrodes herein)

exposed (figure 4 G). The SU8 passivation layer was spun on at 4000 rpm for 30 seconds at a 500 rpm/s ramp rate. It was baked at 90 ^{o}C prior to exposure for 5 minutes, 95 ^{o}C for 1 minute after exposure, before being annealed at 120 ^{o}C for 20 minutes. The finished batch was then divided up into individual arrays, each containing 3 probe layouts of 9 electrodes (as with figures 5 A and B). Probe masks were designed by a previous BEng project under the supervision of Dr. Paul Steenson. Finished arrays were mounted onto printed circuit boards with the electrical interconnects defined using Au wire bonding (figure 5 A). The contacts were made to copper leads via disks, silver epoxied into place, to aid the bonding process. Both the copper leads and the Au wire bonding were passivated with nail varnish. The practical work in this section (excluding wire bonding) was completed by Dr. Chris Russell.

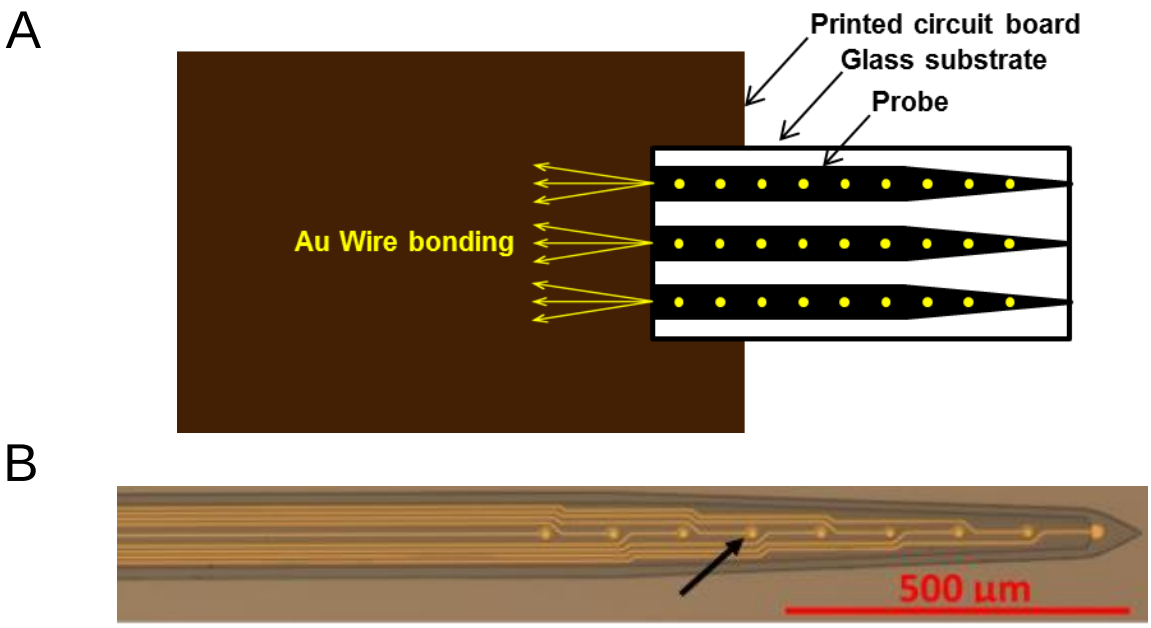

Figure 5 Electrode layout and design. A is a diagram showing how the glass substrate, with the electrode arrays printed on its surface, was mounted onto a printed circuit board. Wire bonding connected electrode arrays and printed circuit board. B is a picture of an intra-spinal /cortical probe shaft fabricated with the same mask used to fabricate the microelectrodes. The Au interconnects are clearly visible under the 1-µm-thick SU8 passivation layer. They terminate with the round, 14-µm-diameter Au electrodes. Arrow highlights example electrode. Note the 14-µm-diameter surrounded by the 20- µm-diameter Au below the passivation layer suggesting successful undercut profile. Presented with permission from Dr. Chris Russell.

3.2.3 Roughened Surface (Chips) Fabrication

Roughened SU8 and Au surfaces, or 'chips', were fabricated for biocompatibility tests. The fabrication procedure was identical to electrode array fabrication (section 3.2.2), excluding all photolithographic steps. The process is outlined schematically in figure 3: A 25 x 25 x 0.2 mm glass Corning cover slip was used as a host substrate for the whole process. Onto this, a 2-µm-thick layer of SU8 was spun, exposed and cured (figure 6 A), as per manufacturer guidelines. The SU8 was then nano-roughened using RIE (see section 3.2.2; figure 4 B & figure 6 B). As mentioned, radiofrequency power of the oscillating magnetic field applied determined the roughness. In this study, as with electrodes, surfaces are referred to by their RIE power. After SU8 roughening, a 10-nm-thick adhesion layer of titanium metal was deposited, followed by a 100-nm-thick layer of Au (figure 6 C). This step was skipped when fabricating the SU8 chips. The roughened SU8 and Au surfaces were then divided up into chips. This work was completed by Dr. Chris Russell.

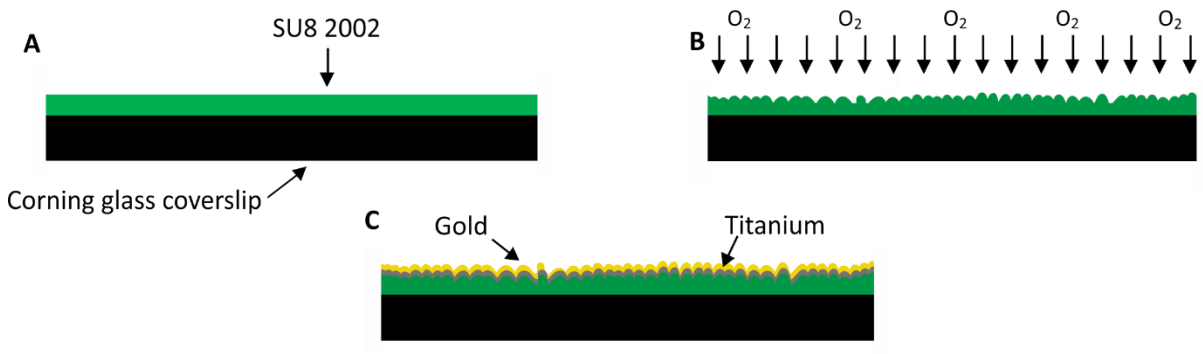

Figure 6 Simplified schematic diagram outlining the roughened surface (chips) fabrication process. A) 2 µm thick layer SU8 2002 was spun and cured on a glass coverslip. B) SU8 was roughened using reactive ion etching. C) Titanium and then gold was deposited. Step C was skipped for fabrication of the rough SU8 surfaces.

3.3 Surface Roughness Characterisation

AFM (atomic force microscopy) was used to characterise the surface of the Au chips. As the roughening process for chips and electrodes was identical, an identical surface roughness was assumed in discussion. In AFM, a tip is drawn over a surface and the change in height

is measured giving a 2 dimensional surface profile. A 3 dimensional surface profile is obtained by scanning the tip over the entire surface in rows. A 10 nm diameter OTESPA tip (Veeco) was used in tapping mode (drive frequency 293 Hz), scanning a 4 μm^2 area with a resolution of 640 samples per row, across 640 rows. For each area the mean averaged roughness (Ra) and the root mean squared averaged (Rms) area roughness are assessed. Each sample was scanned three times and averaged (means with standard deviation). This work was completed by Dr. Chris Russell.

3.4 Electrochemistry

3.4.1 Setup

All measurements were performed with a three electrode setup (figure 7), using a PalmSens3™ potentiostat. Data was recorded onto a computer using PSTrace™. The first electrode was a counter electrode consisting of a standard size (25 x 75 mm) glass microscope slide with platinum (Pt) deposited onto one side. Second, working electrodes

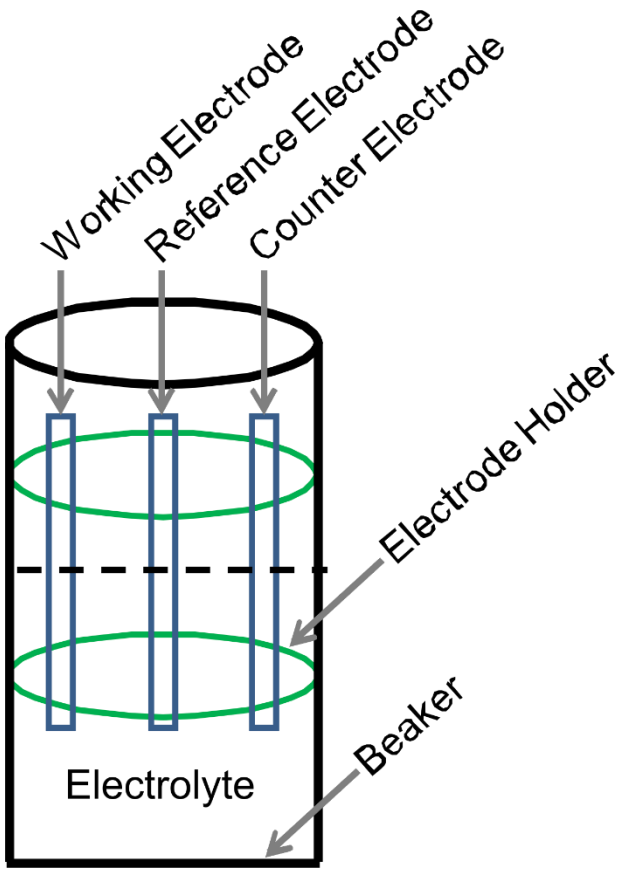

Figure 7 Schematic diagram of the electrode characterisation setup.

were fabricated as above (section 3.2.2). Third, a Ag|AgCl 3 M KCl glass reference electrode (Aldrich®). All potentials reported are with respect to Ag|AgCl. As shown in figure 7, measurements were conducted in a 100 mL glass beaker which was washed with de-ionized water between each use. A custom built holder was used to ensure working and counter electrodes were submerged a consistent amount for each measurement. Approximately half of the counter electrode was submerged in electrolyte, whilst the working electrode was submerged to approximately 0.5 cm above the top of the array. The electrolyte was filled to a mark on the beaker to ensure consistency. At the start of both cyclic voltammetry and electrical impedance spectroscopy scans the open circuit potential (OCP) is used as a baseline potential difference between the counter and reference electrode. Both therefore require a constant OCP in order to provide comparable results between scans. For this reason, at the start of each session OCP was measured until it remained constant with fluctuations of less than 10 mV in amplitude. All measurements were performed at room temperature.

3.4.2 Electrical Impedance Spectroscopy

In electrical impedance spectroscopy (EIS), a potential difference created between the working and counter electrode and impedance is calculated from the current response at the working electrode. This is done by, first, applying a DC (direct current) bias between the counter and working electrode, in this case set at 0 V relative to the OCP to ensure that there was no current due to depolarisation (Zaidi et al. 2010).. Then, a sinusoidal voltage (0.1 V amplitude) was applied over a range of frequencies between the counter and working electrodes. As shown in figure 8 A, there were 41 frequencies tested over a logarithmic range (1 Hz – 10 kHz) (Heim et al. 2012). Data points were plotted starting at the highest frequencies, working down.

The impedance at each frequency was measured 4 times. As shown by figure 8 A, the first scan through all measured frequencies was different from the rest due to lower concentration of ions in the diffuse layer around the electrode (see section 2.1), so it was not taken for analysis. This was not the case with the final 3 scans, so they were taken for analysis. All analysis of impedance data was for 1 kHz, since it is the mid-range of

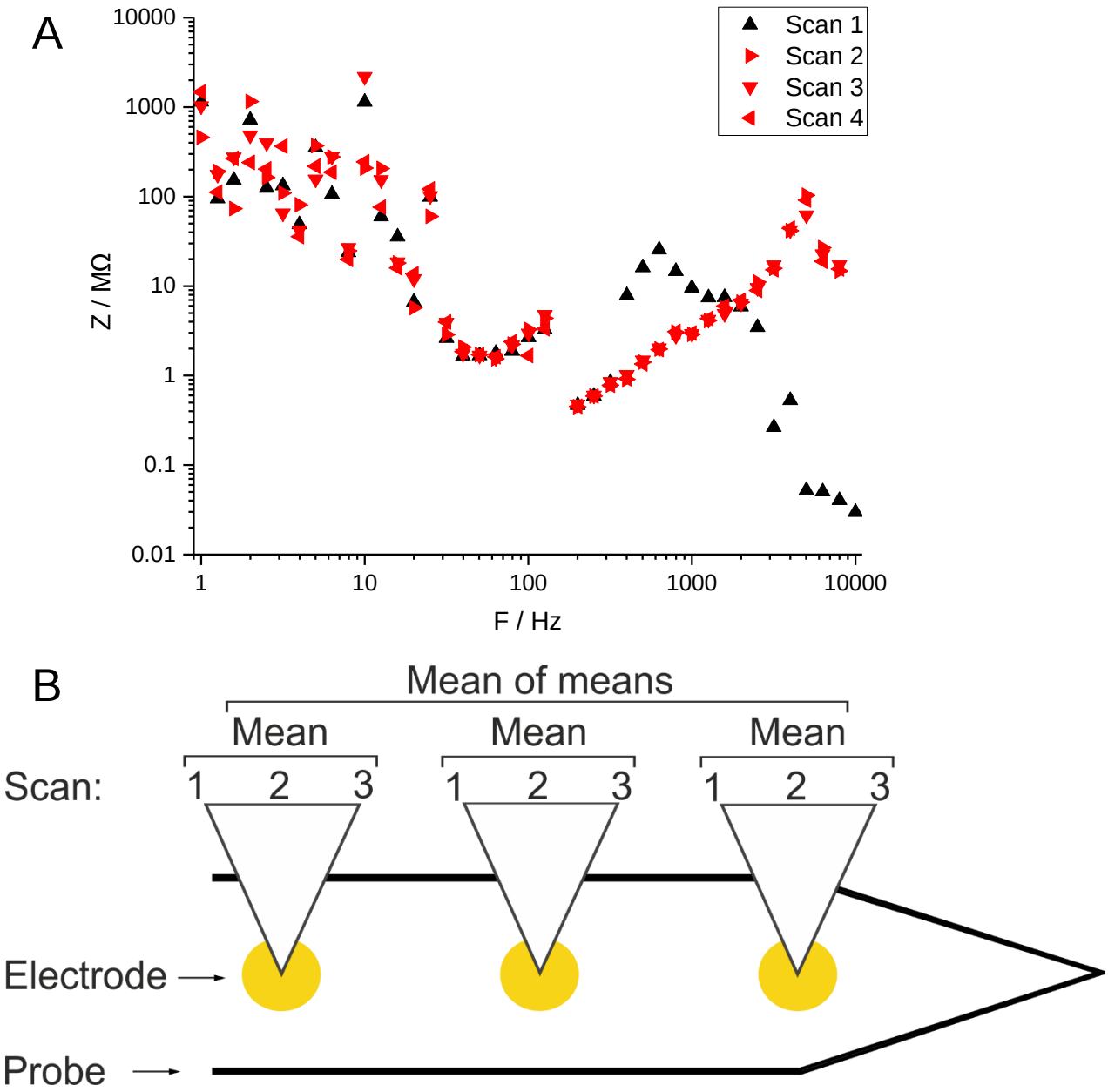

Figure 8 Last 3 electrical impedance scans used for analysis. A is an example electrical impedance spectra: the first scan (black) differs from the other 3 (red). Impedance was measured at 41 frequencies between 1 Hz – 10 kHz. B is a schematic illustrating how the data was analysed. Each probe had one degree of roughness. The mean 1 kHz impedance was taken from each electrode. Mean of means was calculated for each degree of roughness.

biologically relevant frequencies of neural activity (Negi et al. 2010). As in figure 8 B, the mean 1 kHz impedance was calculated from the three scans for each electrode. A mean of means was then calculated for each electrode array. All measurements used to compare impedance between degrees of roughness conducted before cyclic voltammetry (CV) measurements. This was to avoid potential effects cyclic voltammetry may have. All impedance measurements comparing the effects of protein adhesion were done after cyclic voltammetry.

3.4.3 Cyclic Voltammetry

The charge storage capacity (CSC) of each electrode array was measured using CV. In CV, the counter electrode scans between two potentials and the current response of the working electrode is measured. CSC is the maximum amount of charge that can be stored at the electrode surface before hydrolysis and the production of gasses (i.e. H_2 and O_2 evolution). To establish the voltage window within which no hydrolysis occurs, CV was conducted on a non-roughened working electrode array. Starting at ± 0.5 V, the potential window was incrementally increased by ±0.1 V between each CV. As with all CV measurements in this study, CVs started at +0.5 V (relative to open circuit potential) and swept positively first with a sweep rate of 50 mV/s (Ghazni et al. 2010; Hu et al. 2006). A slow scan rate was used to measure the maximum amount of charge the electrode was able to deliver. DC bias was set 0 V vs the open circuit potential to ensure that there was no current due to depolarisation (Zaidi et al. 2010). Sharp increases of either anodic or cathodic current were taken to be as a result of going outside the hydrolysis window (García-Gabaldón et al. 2011). As shown by figure 5 A, a sharp anodic current increase occurred at ~ +1.1 V, implying that it is outside the minimal voltage limit of hydrolysis. To accommodate for any between electrode variations, a voltage window ± 0.2 V smaller than the upper limit was used. Therefore, all CV measurements were conducted between ±0.9 V.

Each electrode underwent 4 CV scans for each CSC measurement. As illustrated by figure 9 B, the first CV scan was typically different from others. For this reason, the first was ignored and the following 3 were taken for analysis. The mean CSC for each electrode was calculated by averaging these 3 scans. As in figure 5 C and D, both anodic (CSCa; figure 9 C) and cathodic (CSCc; figure 5 C) charge was first calculated from the size within either the

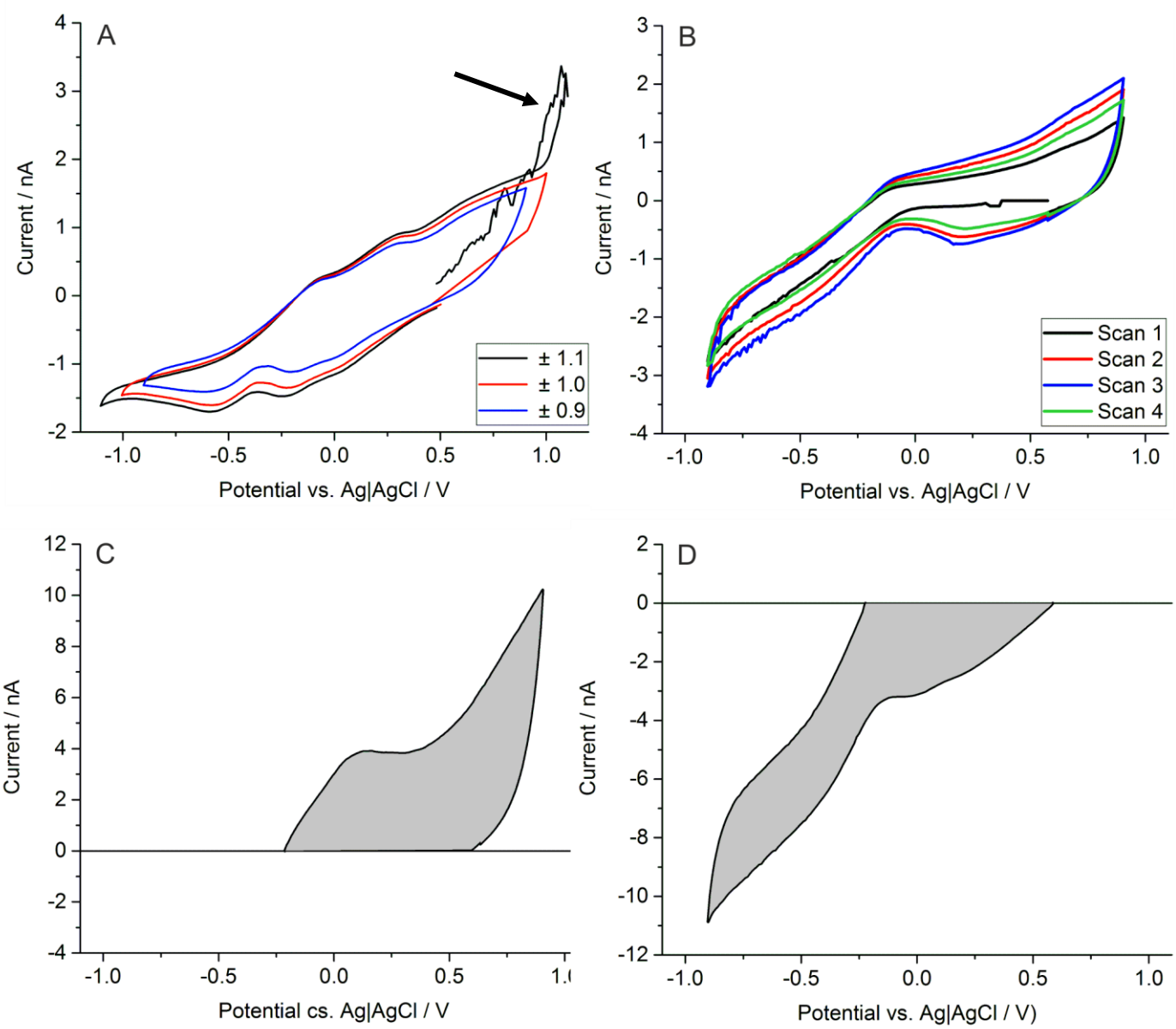

Figure 9 CV optimisation and analysis. A is a cyclic voltammograph demonstrating the effects on CSC of increasing the voltage. The arrow highlights ± 1.1 V sharp anodic increase, implying hydrolysis. B is a cyclic voltammograph demonstrating the difference between the first of 3 scans of the same electrode in comparison to the other two. C and D are examples of how the anodic (C) and cathodic (D) CSCs are measured from a single CV scan. The shaded regions are the area measured.

positive (CSCa) or negative (CSCc) regions within the CV scan. This was done using the 'Polygon Area' function in Origin. CSC was then calculated by dividing this by the geometric surface area of the electrode. The CSC for each array was calculated by averaging the electrodes CSCs (mean with standard error), after removing statistical outliers ($p<0.05$). Outliers were found using GraphPad software. All measurements comparing the impedance between degrees of roughness were conducted before all cyclic voltammetry measurements. All measurements comparing impedance change following incubation with protein solution were conducted after all cyclic voltammetry measurements.

3.5 Tissue homogenisation and BCA

A protein solution was made to model biofouling. This process is summarised in figure 10. Proteins were extracted from the brain of a healthy male Wistar rat weighing between 200 – 300 g. The brain was removed immediately after termination. All procedures were approved by the UK Home Office and performed under the Animals (Scientific Procedures) Act 1986. The sample was weighed and placed with 25 ml chilled RIPA (Radioimmunoprecipitation assay – see table 1) buffer before being homogenised by a Cole-Parmer ® LabGen 125 tissue homogeniser. A SIGMA*FAST*™ protease inhibitor cocktail tablet was then added according to manufacturer's instructions. The sample was centrifuged at 1,000 *g* for 10 minutes at 4°C, and the supernatant was collected. The protein concentration of the solution was then quantified using a Pierce ™ BCA (bicinchoninic acid) protein assay: Five BSA (bovine serum albumin) dilutions (5, 25, 50, 125 and 250 µg/mL) were made in de-ionised

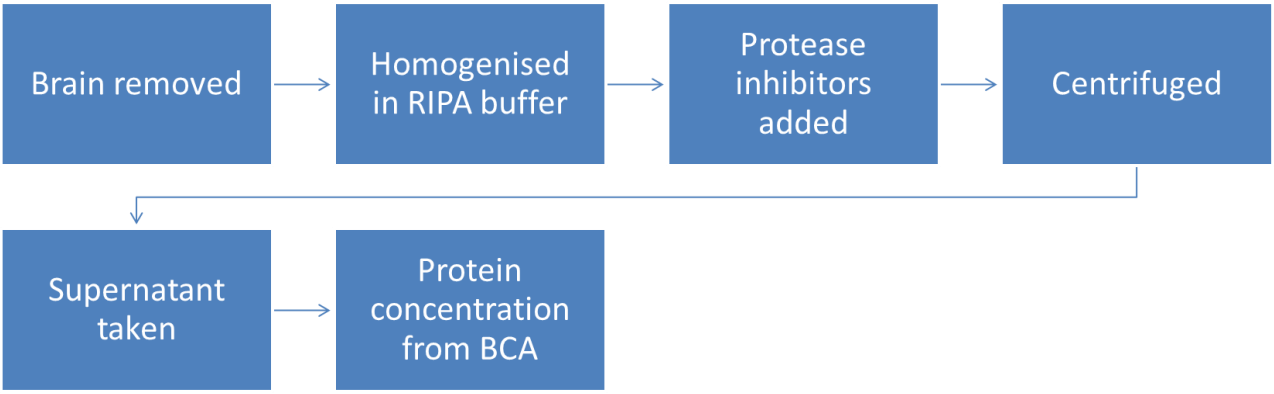

Figure 10 Summary of the protein extraction process.

water. BCA working reagent was prepared by mixing 50 parts BCA reagent A with 1 part BCA reagent B, as per manufacturer's instructions. Working reagent was then added to both the sample and BSA standards (1:20, sample:working reagent) and incubated at 37^{o}C for 30 minutes. Using a de-ionised water control, BSA standards and protein samples were then plated in duplicate. The absorbance at 562 nm was taken using a Varioskan Flash Spectral Scanning Multimode Reader (Thermo Scientific^{TM}). Analysis was done using SkanIt^{TM} 2.5.1 software (Fisher®). Using Microsoft Excel®, the average absorbance of each of the BSA standards minus the average absorbance of the water was plotted against concentration. The standard curve generated was used to estimate the sample protein concentration (please see Appendix 1, figure 28).

3.6 Impedance Following Incubation with Protein Solution

To model the effects of biofouling, impedance was compared before and after incubation with protein solution.

3.6.1 RIPA Buffer Protein Solution

Baseline impedance was again measured (as above; figures 7 & 8) for all electrodes on each electrode array. This was done after cyclic voltammetry. As the protein solution contained RIPA buffer, it was necessary to control for any potential effects the RIPA buffer may have on electrode impedance. As outlined in figure 11, arrays were incubated with 35 µL 1 X RIPA (Radioimmunoprecipitation assay) buffer on their surface for 2 hours at room temperature after the baseline measurements. For all measurements in this and the following section (3.6.2), only aCSF was used as an electrolyte. For each electrode array, the beaker containing the electrolyte was sealed with para-film and reused for the measurements post incubation. With the RIPA buffer still on the electrode array surface, the arrays were lowered carefully into the electrolyte. Impedance measurements were repeated in the same order as before. For each electrode, the difference between scans before and after incubation with the protein solution (i.e. scan 1 after – scan 1 before, scan 2 after –

scan 2 before) was calculated. This difference was considered due to RIPA buffer incubation. The electrode arrays were rinsed thoroughly with de-ionised water using a squeeze bottle and left to dry overnight. This process was then repeated with RIPA buffer containing protein replacing just RIPA buffer (figure 11). To establish the effects the protein had on impedance, the difference from RIPA was taken away from RIPA + protein, giving the following: change from RIPA + protein – change from RIPA = change from Protein. The mean of these values were calculated for each electrode, and the outliers ($p<0.05$) removed. The mean of all electrodes (excluding outliers) was calculated for each array and is given (± standard error).

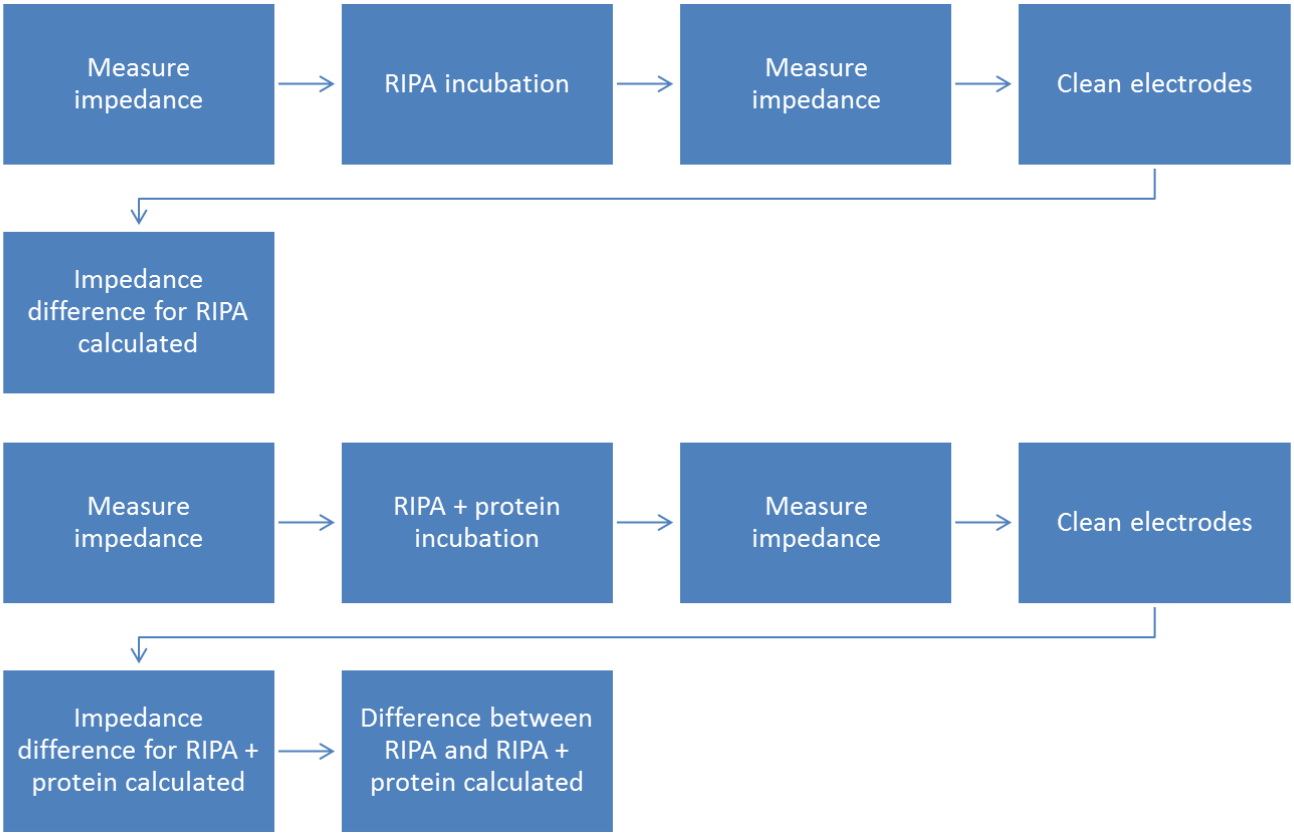

Figure 11 Experimental process for the RIPA buffer protein model.

3.6.2 aCSF Protein Solution Including Dialysis

aCSF protein solution was also used as aCSF is a more biologically accurate solute compared to RIPA buffer. As with the previous section, only aCSF was used as an electrolyte. As summarised in figure 12, dialysis was used to replace the RIPA buffer with

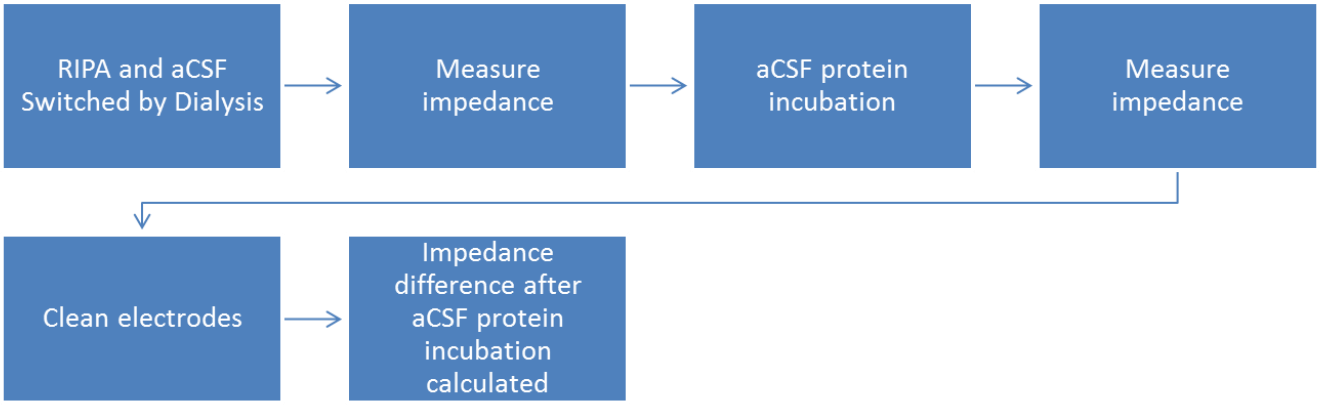

Figure 12 Experimental process for the aCSF protein model.

aCSF: 1.5 mL RIPA protein solution was transferred into dialysis tubing (Sigma®). The tubing was sealed at both ends with klippits and was left in 2 L 1 x aCSF overnight at 4^{o}C. The volume of the resulting solution was obtained and concentration calculated. Impedance was measured before and after 2 hour incubation with 35 µL of aCSF protein solution at room temperature on the electrode array surface. As mentioned (section 3.6.1), impedance measurements for each electrode were conducted 3 times. Change in impedance for each electrode was calculated by the difference between each of the 3 corresponding scans before and after incubation (i.e. scan 1 after – scan 1 before, scan 2 after – scan 2 before). The mean of these values was calculated for each electrode, and the outliers ($p<0.05$) removed. The mean of all electrodes (excluding outliers) was calculated for each array and is given (± standard error).

3.7 Biocompatibility

Neu7 and A7 astrocytic cell lines were cultured separately on both SU8 and Au chips to model in-vivo cellular response to electrode arrays with differing degrees of roughness.

3.7.1 Cell Culture, Plating and Immunohistochemical Staining

Cell culturing and incubation with the chips was conducted using Dulbecco's modified Eagle's Medium (DMEM) with 4.5 g/L glucose, 30 mg/L L-glutamine and 10% Fetal Bovine Serum (FBS) in 37^{o}C, 4% CO_2. To concentrate cell solution on the chip surface during plating, wells were constructed from PDMS (Sylgard 184; Dow Corning).The Sylgard was

mixed 10 parts elastomer base to 1 part curing agent, poured into a 150 mm diameter petri dish, degassed and cured in a vacuum oven at 80°C for 2.5 hours. The resulting object was then cut up, and wells were made by cutting a hole using a surgical scalpel. This was done around a stencil (0.7 x 1 cm) to ensure the chips were submerged under a consistent amount of media during incubation (figure 13 A). As in figure 13 B, both chips and PDMS wells were then decontaminated by submerging in 70% ethanol at room temperature for 10 minutes. They were then transferred into the fume hood and dab dried on tissue paper before being rinsed using de-ionised water rinse and drying process was repeated twice. The bases of the PDMS wells were sealed with Dow Corning High Vacuum Grease. To

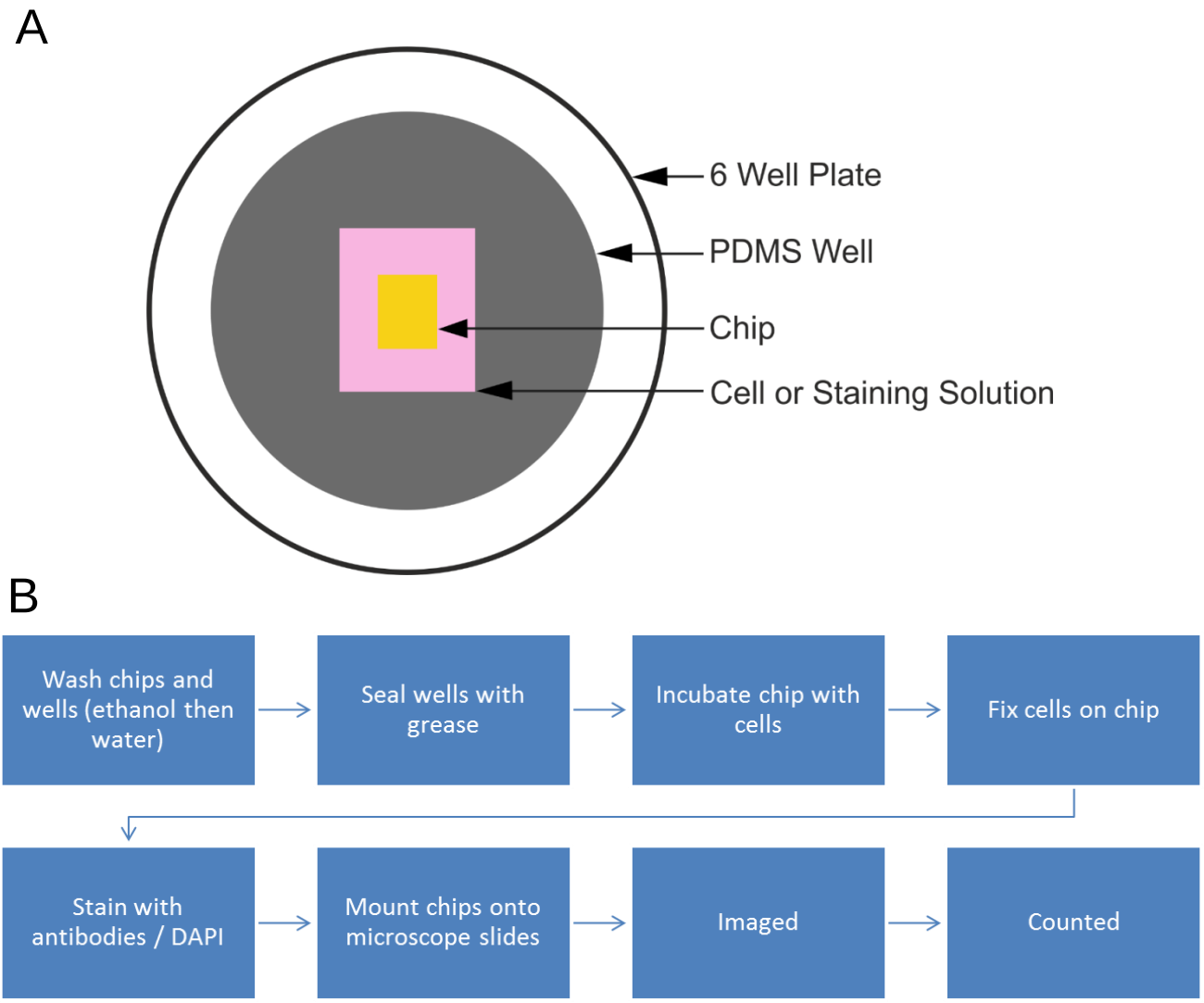

Figure 13 Cell culture / staining process. A is schematic diagram of experimental setup used to culture the cells. Cells were cultured and stained on the test surfaces (chips) in custom made PDMS wells in 6 well plates. B is a simplified flow chart of the culture, staining and counting process.

encourage cell attachment, chips were incubated with polylysine at room temperature for 1 hour. The polylysine was then removed and the chips were left to dry overnight in the fume hood. Cells were plated and incubated in 37^{o}C, 4% CO_2 for 5 hours. Neu7 and A7 cells were plated on different chips so that only one cell line was on each chip. Both lines were plated in the same concentration (100,000 cells/ml). This concentration was found to give the optimal confluency (~ 60%) during optimization.

After incubation, media was removed and the chips were transferred to a 48 well plate for staining. Chips were washed once in PBS (10 minutes) and incubated for 15 mins in 4% Paraformaldehyde (200 µL/well) at room temperature. Chips were then washed 3 times in 1 x PBS before being blocked by PBS containing 0.2% Triton (PBST) with normal donkey serum (NDS) (3% volume) for 1 hour in room temperature. Next, the solution was replaced with PBST, containing 3% NDS and Anti-GLAST1 (glutamate asparate transporter; highly glial selective membrane protein) primary antibody before being incubated for 18 hours in the dark at 4^{o}C. After being washed in PBST 3 times, chips were then incubated with 200 µL/well of the PBST-NDS mix containing the anti-mouse Alexa fluor 568 secondary antibodies for 2 hours in the dark at room temperature. Chips were washed in PBST once, before being incubated with PBS containing DAPI (1:2000 dilution) for 2 minutes at room temperature in the dark. Finally, chips were washed once in PBS before being mounted onto slides using fluoromount G mounting medium. This process is summarised in figure 13 B.

3.7.2 Cell Counting

Cells were imaged using a LSM 700 (Zeiss) laser scanning confocal unit attached to an inverted Axio Observer (Zeiss) microscope with an EC Plan-Neofluar 20x objective (NA = 0.5). Images were captured at a 128 x 128 pixel definition and visualised using Zen Black (version 8.1) software. An argon laser was used to provide excitation at 405 nm (DAPI - blue) and 555 nm (Alexa flour 568 - red). Cells were counted from a 64 image tile scans (8 x 8 images; figure 14) of equal size. Each chip had only one tile scan, taken of a random location on the chip surface. DAPI stain was used to count the cells in each tile in ImageJ.

Staining was taken to be cells if 3 criteria were fulfilled: First, it was within the chip perimeter. Second, DAPI staining overlapped with Alexafluor 568 and the DAPI stain was within the Alexafluor 568, as with figure 14 insert. Third, if the DAPI stain was within a defined area range. The DAPI area range (Neu7: 32 - 80 μm^2 A7: 22.4 – 64 μm^2) was defined for each cell line by measuring the largest and smallest nuclei for that cell line across multiple tiles. DAPI images were converted to black and white and the defined size range was used to count nuclei using the 'Analyse Particles' function in ImageJ. As in figure 14, this method was validated for each cell line by overlaying the counted nuclei with the Alexafluor 568

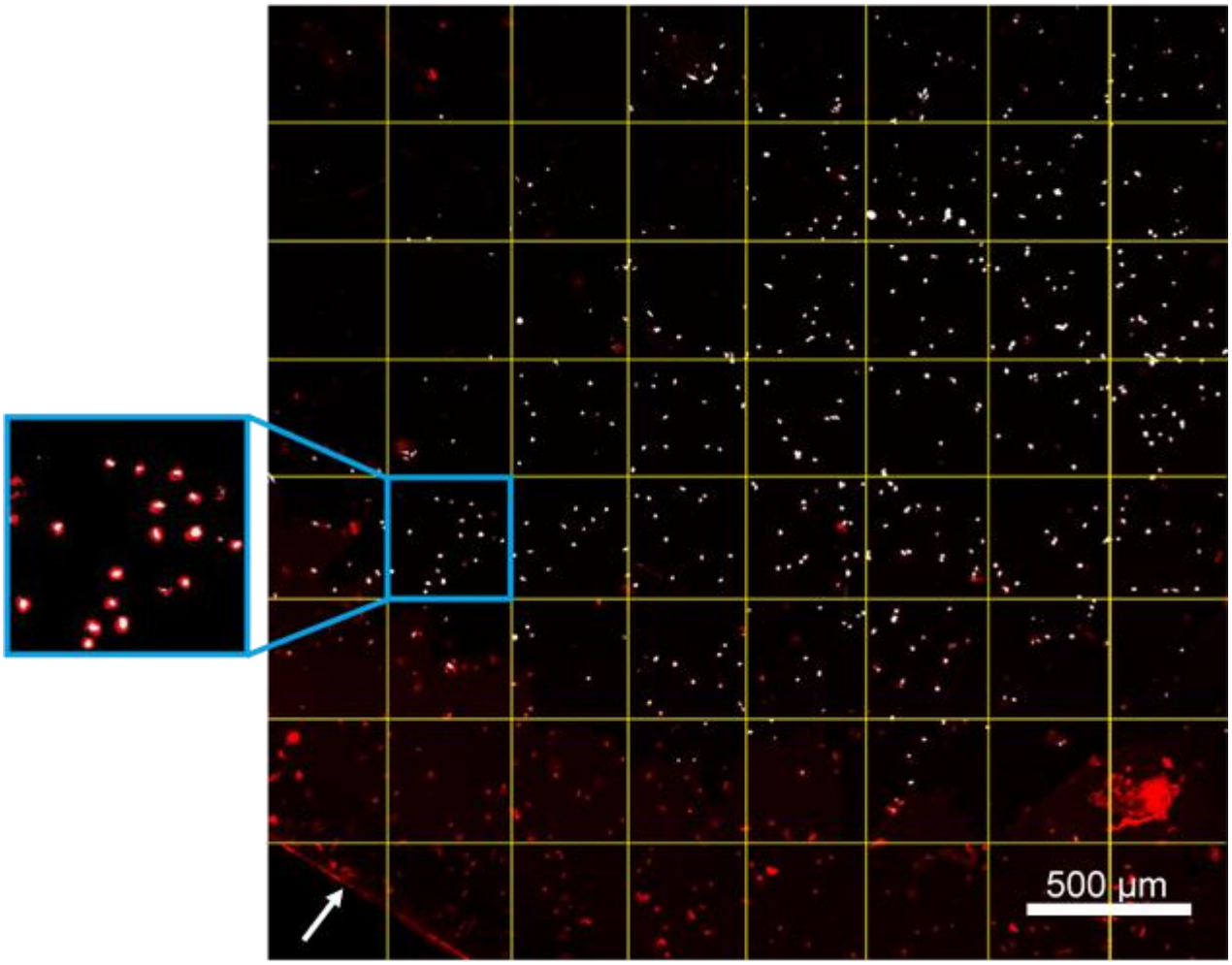

Figure 14 Example tile image with counted DAPI stained nuclei (white – pseudo colour) overlaying Alexafluor 568 stained cell bodies (red). Tile is divided into 64 squares to allow for subtraction of regions outside of the chip. White arrow highlights edge of chip. Insert magnification shows how DAPI stain is within the cell body.

image, and size range was adjusted accordingly. Due to the random process of which parts of the chips surface image, regions outside of the chip were sometimes imaged (figure 14 gives an example). To account for this (as in figure 14), tile images were divided into 64 squares of equal size and the average cell density (i.e. cell count / square count) was calculated. Squares containing regions outside of the chip were not included. Cells within those squares were also not included.

3.8 Statistics

All ANOVA and correlations were done using Origin software. For all correlations, data points qualified as outliers if they were 1.5 * the interquartile range (calculated in Origin) outside of either the upper or lower quartiles (Devore et al. 1999). Alternative correlations are given to establish whether outlier removal increased correlation strength.

Chapter 4: Results

Au and SU8 roughened to different degrees were tested in several different scenarios to establish which degree of roughness may be the optimal choice for enhancing electrode performance.

4.1 Surface Roughness Characterisation

The effects of surface roughening using different RIE plasma power values on the degree of roughness of Au (gold) surfaces were measured using atomic force microscopy (AFM). As shown in figure 15, Au surface features increased in size with RIE power. Figure 16 shows how roughness increases with increasing RIE power. This data was collected and analysed by Dr. Christopher Russell. It has been included in this thesis as a baseline, allowing us to compare the surface roughness values - as opposed to just the RIE power - to other results. Figure 16 includes both Ra and Rms roughness. Since both Ra and Rms are different ways of analysing the same data, only Ra has been used to compare degrees of roughness to other results since it is used in previously published literature (Chung, et al. 2015; Bhandari et al. 2011).

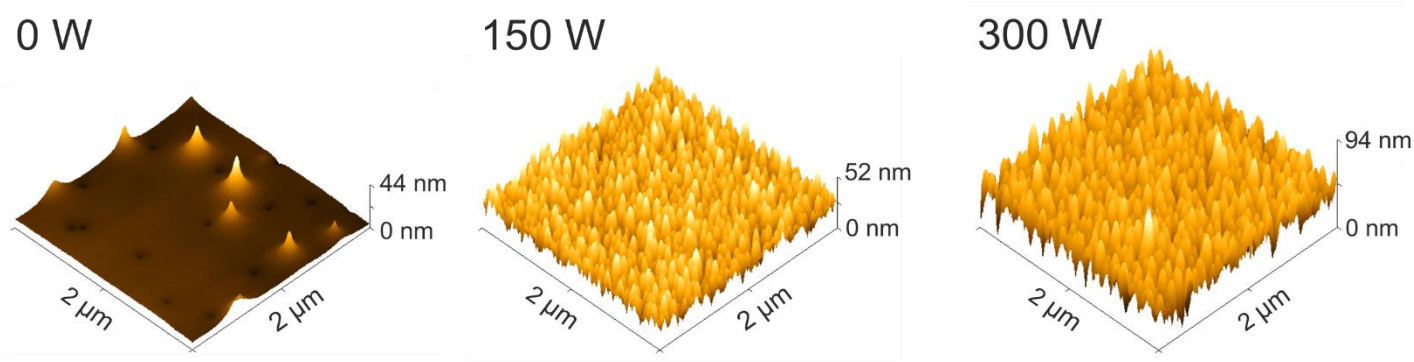

Figure 16 Example 3 dimensional representations of AFM scans. Surface features increase in size with greater RIE power.

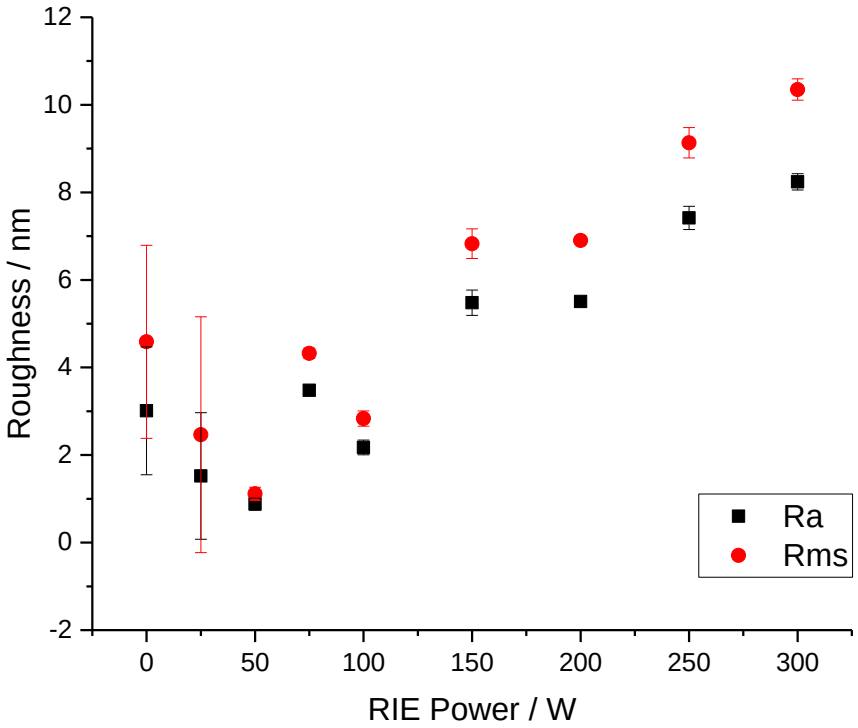

Figure 17 Measure of roughness of Au chips for each roughening power. The roughness was measured as average roughness (Ra) and root mean squared (Rms) in nm (± SD) and the mean of 3 measures per chip. This work is presented here with the permission of Dr. Chris Russell.

4.2 Electrode Impedance

The number of electrodes recorded from for each degree of roughness is listed in table 2. Electrode impedance was compared for all degrees of roughness. The objective was the find the degree of roughness with the lowest impedance. The effect of surface roughening on electrode impedance was measured in both aCSF and PBS. Figure 17 A and B give the mean impedance (at 1 kHz) for each degree of roughness in both aCSF (figure 17 A) and PBS (figure 17 B). Roughening significantly increased ($p<0.05$; 1 way ANOVA, Bonferroni's post hoc) impedance in aCSF for all degrees of roughness, except 200 W. 200 W had a

Table 2 The number of electrodes used for measurements for each degree of roughness

RIE Power (W)	0	25	50	75	100	150	200	250	300
Electrodes	4	8	7	7	7	7	8	4	0

significantly lower impedance than 25, 50, 100 and 150 W, implying 200 W is the most desirable degree of roughness.

Roughening significantly increased impedance measured in PBS for 25 and 150 W in comparison to 0 W ($p<0.05$; 1 way ANOVA, Bonferroni's post hoc). 150 W was also significantly higher than 50, 75, 100 and 200 W. This suggests that when measured in PBS, 150 and 25 W are the least desirable degrees of roughness. Correlations were performed to establish if there was any relation between roughness and impedance (figures 17 C and D). They were done using the Ra roughness values in figure 16. As shown, there was no correlation between impedance measured in either aCSF (figure 17 C; $r^2 = 0.006$) or PBS (figure17 D, $r^2 = 0.03$).

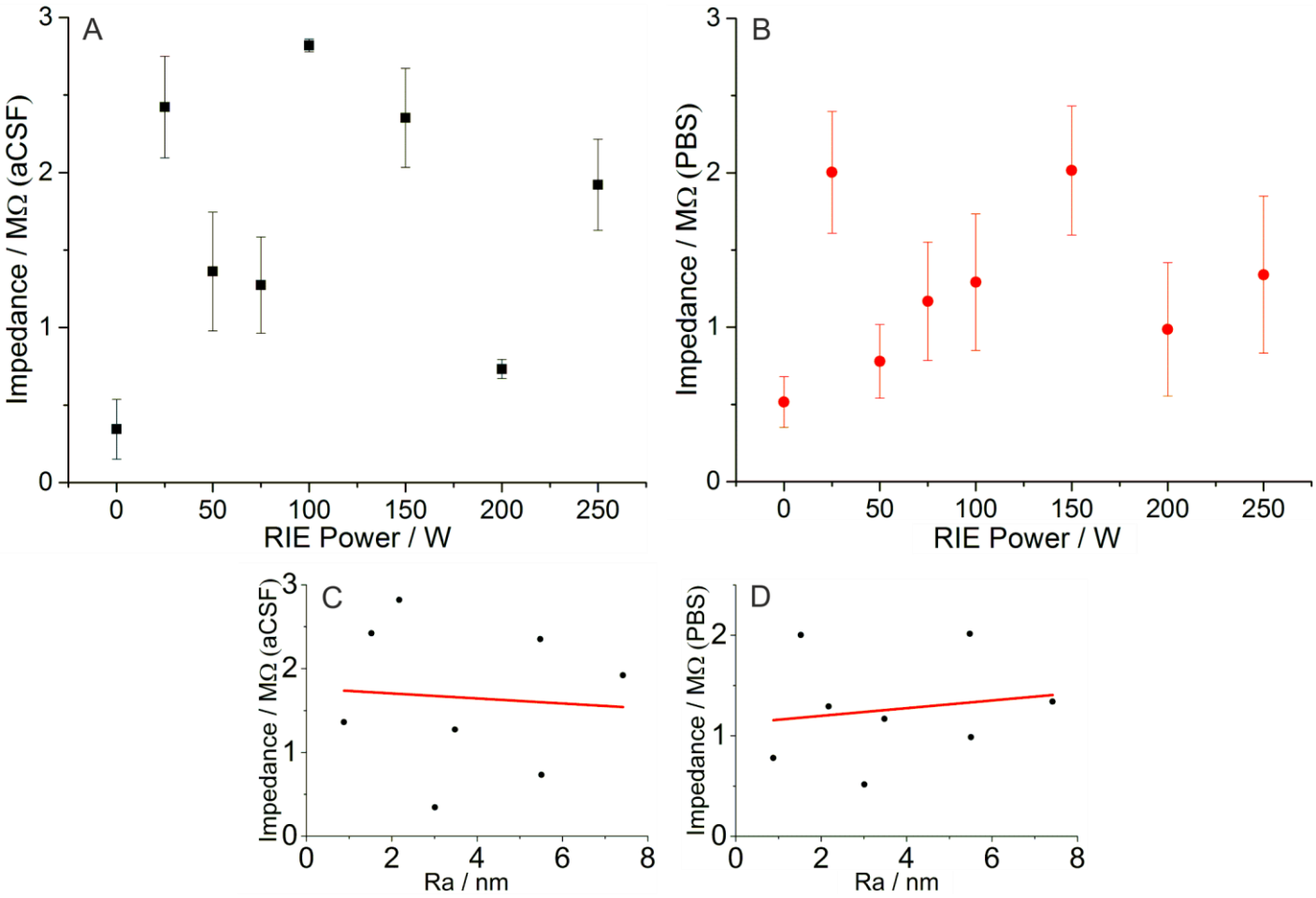

Figure 18 The impedance measured at 1 kHz for each array (mean ± SEM). Electrolyte was either aCSF (A) or PBS (B). For n numbers see table 2. C is impedance correlated against Ra measured in aCSF. D is the correlation between Ra and impedance in PBS.

4.3 Charge Storage capacity

To assess whether roughening had enhanced our electrodes potential to stimulate neural activity, cyclic voltammetry (CV) was used to measure the charge storage capacity (CSC) of each electrode array. The objective was to find the degree of roughness with the highest CSC. CSC is divided into cathodic (CSCc) and anodic (CSCa). Figures 18 A and B give the mean CSCa for each degree of roughness measured in aCSF (figure 18 A) and PBS (figure 18 B). In both aCSF and PBS, 50 W was the only roughness to have a significantly greater CSCa than others suggesting it is the optimal degree of roughness for increasing CSCa ($p < 0.05$, one way ANOVA, Bonferroni post hoc). Ra was correlated against CSCc and CSCa to establish if there was any relation between roughness and CSC. There was no correlation between CSCa measured in aCSF and either Ra with (figure 18 C, $r^2 = 0.42$) or without

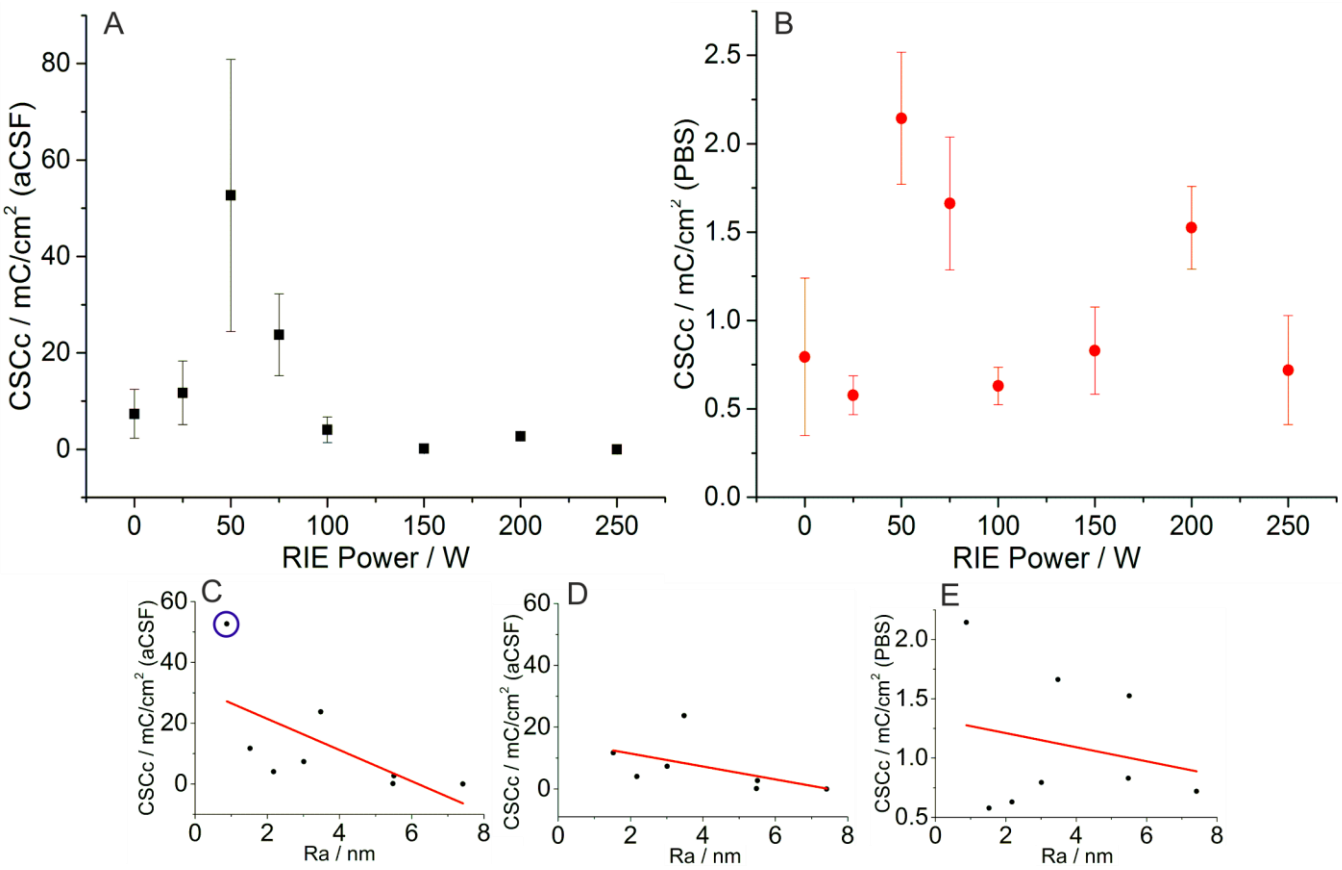

Figure 19 Anodic CSC (CSCa) data. A and B are the CSCa (mean ± SEM) for each array, using either aCSF (A) or PBS (B) electrolyte. For n numbers see table 2. C and D are the correlations between Ra and CSCa in aCSF with (C) and without (D) outliers. E is CSCa in PBS correlated against Ra. Outliers are circled in blue. See text for r^2 values.

outliers (figure 18 D, r^2 = 0.27). There was also no correlation between Ra and CSCa measured in PBS (figure 18 E, r^2 = 0.09).

Figures 19 A and B give the mean CSCc for each degree of roughness measured in aCSF (figure 19 A) and PBS (figure 19 B). In aCSF, there was no statistical difference between any degrees of roughness (one way ANOVA, Bonferroni post hoc). However in PBS, 50 W was significantly larger than all other values, and 75 W was significantly larger than all values except 0, 25 and 50 W. 200 W was also significantly larger than 0 W (one way ANOVA, Bonferroni post hoc). CSCc measured in aCSF did not correlate against either Ra with (figure 19 C, r^2 = 0.21) and without (figure 19 D, r^2 = 0.68) outliers. CSCc measured in PBS also did not correlate against either Ra with (figure 19 E, r^2 = 0.25) and without (figure 19 F, r^2 = 0.23) outliers.

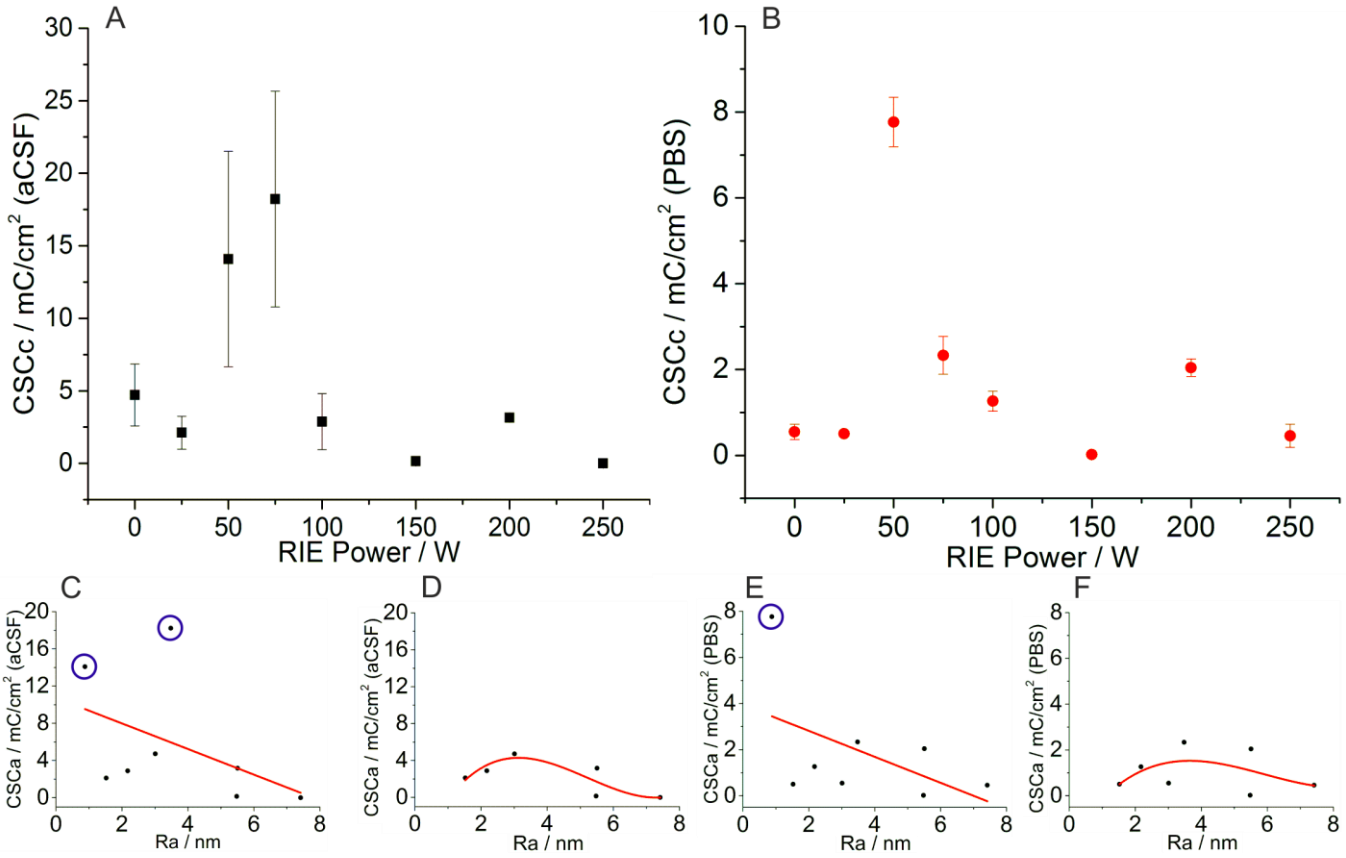

Figure 20 Cathodic CSC (CSCc) data. A and B are the CSCc (mean ± SEM) for each array, using either aCSF (A) or PBS (B) electrolyte. For n numbers see table 2. C and D are Ra correlated with CSCa in aCSF with (C) and without (D) outliers. E and F are CSCa against Ra in PBS with (E) and without (F) outliers. Outliers circled in blue. See text for r^2 values.

4.4 Impedance Change Following Incubation with Protein Solution

Impedance for each RIE power was measured before and after incubation with protein solution. From this, a before vs. after impedance difference was found. Impedance difference was compared between degrees of roughness. The objective was to find the degree with the smallest impedance increase. Figure 20 gives the mean change in impedance for each degree of roughness following incubation with either RIPA or aCSF protein solution. There was no significant change in impedance difference in protein adhesion for RIPA + protein (figure 20 A; one way ANOVA, Bonferroni's post hoc). There was a weak correlation between impedance change from RIPA protein solution and roughness (figure 20 C, $r^2 = 0.88$). The trend implies that for Ra between 1-6 nm, impedance increases with roughening following incubation with RIPA protein solution. However, at

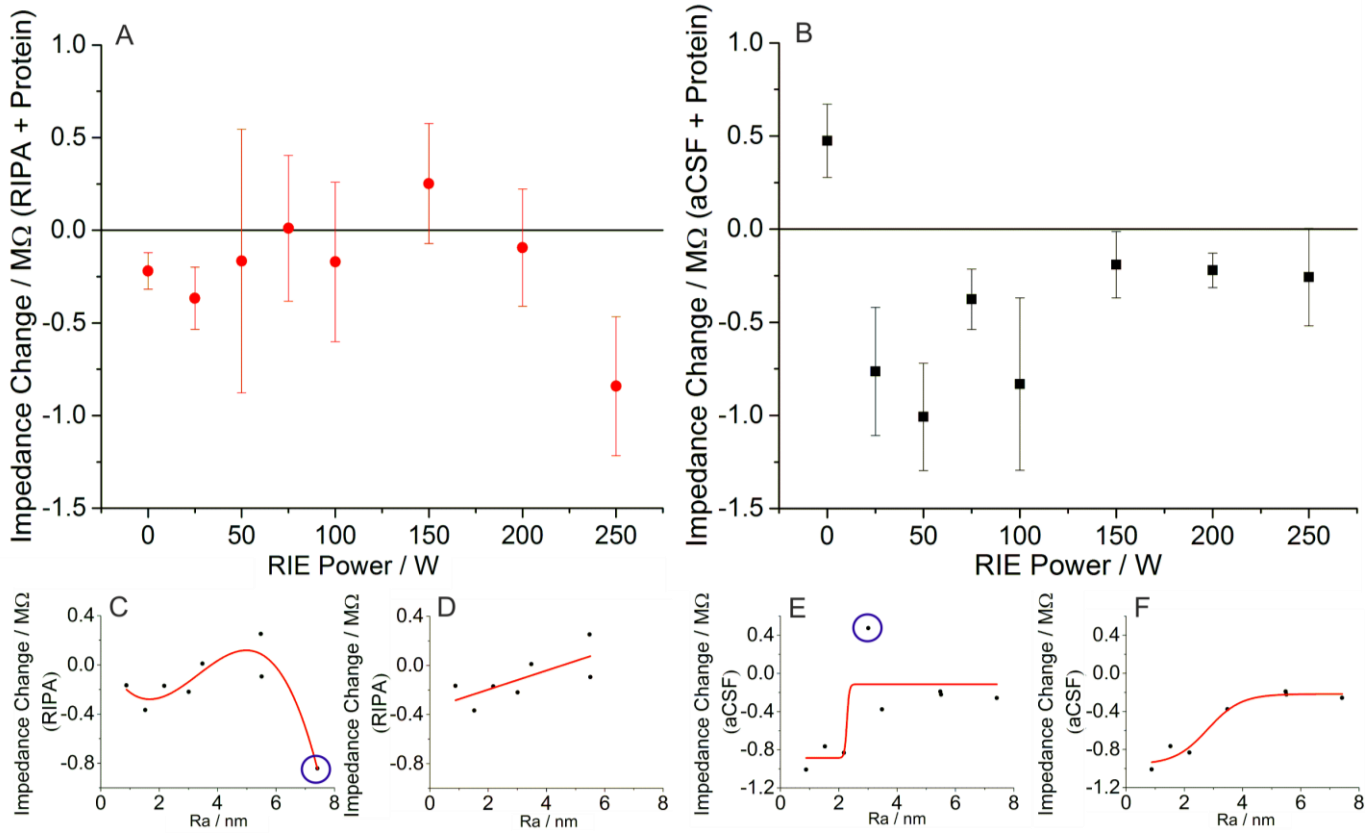

Figure 21 Impedance change for each RIE power following incubation with protein solution. A and B are the impedance change (mean ± SEM) for each array following incubation with either RIPA buffer (A) or aCSF (B) containing protein. For n numbers see table 2. C and D are impedance change from RIPA protein solution against Ra with (C) and without (D) outliers. E and F are impedance change from aCSF solution against Ra with (E) and without (F) outliers. Outliers are circled in blue.

greater degrees of roughness, impedance then decreases. The point causing this decrease corresponds to 250 W, suggesting it is the most desirable degree of roughness for lowering impedance following incubation with RIPA protein solution. Outlier removal reduced association strength (figure 20 D, $r^2 = 0.5$).

Incubation of aCSF protein solution with 25, 50, 75 and 100 W resulted in a significantly smaller impedance increase with time than 0 W (figure 20 B; $p<0.05$; 1 way ANOVA, Bonferroni post hoc), which was the only roughness to increase in impedance. This suggests that all degrees of roughness tested are desirable for reducing impedance increase from biofouling. As highlighted in figures 20 E ($r^2 = 0.69$), 0 W was outlying from the rest of the data. Removal of 0 W outlier creates a strong correlation between roughness and impedance change (figure 20 F, $r^2 = 0.96$). This trend suggests the effects of aCSF protein solution incubation increase with roughness to a plateau at points corresponding to 150 and 200 W. In the same trend, the effects (i.e. impedance reduction) are greatest at 50 W. In line with this, in figure 20 B 50 W undergoes the greatest reduction in impedance. This implies 50 W is the optimal degree of roughness for reducing impedance increase following incubation with aCSF protein solution.

4.5 Biocompatibility

Astrocytic cell lines were cultured on Au and SU8 surfaces, or 'chips', roughened to different degrees and then counted. The amount of chips used for each RIE power in this study is summarised in table 3. Neu7 cells were chosen to model activated astrocytes, whilst A7 non-

Table 3 The amount of chips used for each cell line in this study

RIE Power (W)	0	25	50	75	100	150	200	250	300
Au A7	4	4	4	4	4	4	3	4	4
Au Neu7	4	4	4	4	4	4	3	4	4
SU8 A7	3	0	4	0	4	0	4	0	3
SU8 Neu7	3	0	4	0	4	0	4	0	3

activated (Elizabeth M Powell et al. 1997; Smith-Thomas et al. 1995). A high density of A7 and a low density of Neu7 is therefore desirable (see section 2.3). The objective was to establish which degree of roughness had the highest A7 and lowest Neu7 cell density.

For each degree of roughness, figure 21 A gives the cell density of both A7 and Neu7 cell lines cultured on Au. 25 W had a significantly higher A7 cell density than all degrees of roughness except 100 W ($p<0.05$, one way ANOVA, Bonferroni's post hoc). 25 W A7 cell density was significantly higher than 0, 50 and 150 W, whilst 100 W significantly higher than 150 W, suggesting they are the most favourable. 200 W has a significantly higher Neu7 cell density than all degrees of roughness except 100, 250 and 300 W ($p<0.05$, one way ANOVA, Bonferroni's post hoc). 300 W Neu7 density is significantly higher than 25, 50 and 75 W. This suggests both 300 and 200 W are the least desirable degrees of roughness.

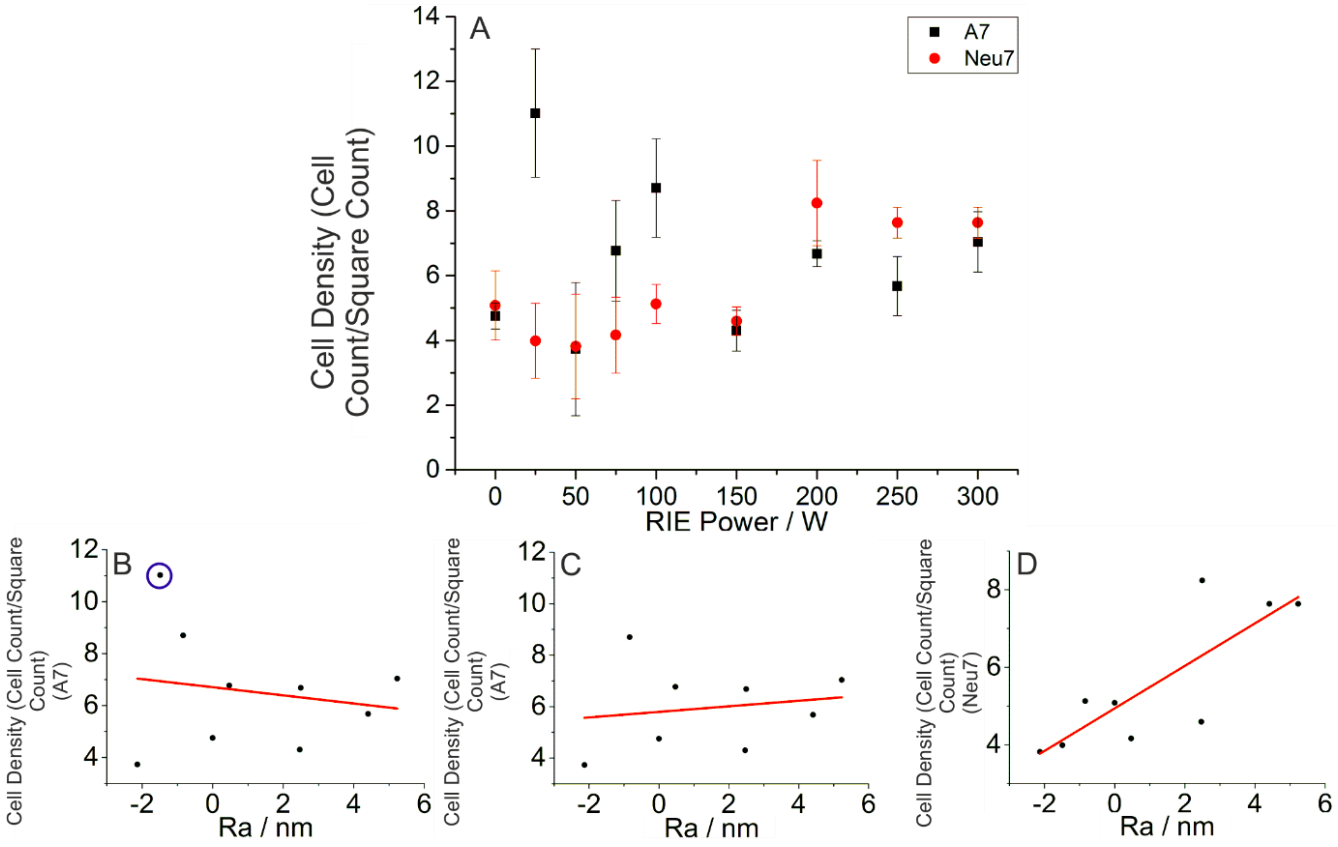

Figure 22 Cell densities counted on Au. A is the A7 and Neu7 cell density (mean ± SD) from 3 different Au chips for different RIE powers. B and C are A7 density correlated against Ra difference both with (B) and without (C) outliers. D is Neu7 density Ra. Outliers are circled in blue.

There was no correlation between roughness and A7 cell density both with (figure 21 B, r^2 = 0.03) and without (figure 21 C, r^2 = 0.03) outliers. This suggests that there is no trend between the degree of roughness and A7 cell survivability. There was a weak correlation between Neu7 and roughness (figure 21 D, r^2 = 0.66), suggesting Neu7 cell density increases with the degree of roughness.

As shown in figure 5B (section 3.2.2), the majority of the probe surface area is SU8. Increasing the biocompatibility of the SU8 surface would therefore be a powerful tool in reducing immune response. The biocompatibility of different SU8 degrees of roughness was compared for this reason. Figure 22 gives the difference in cell density for each degree of roughness for both A7 and Neu7 cell lines cultured on SU8. We did not compare SU8 and Au biocompatibility since we were unable to perform AFM on our roughened SU8 surfaces. Au surface morphology is also likely to be different as it was coated onto roughened SU8. Unlike with Au, A7 cell densities were significantly lower than 0 W for all degrees of roughness except 200 W ($p<0.05$, one way ANOVA, Bonferroni's post hoc). 200 W was significantly greater than all degrees of roughness, except 0 W. There was no significant

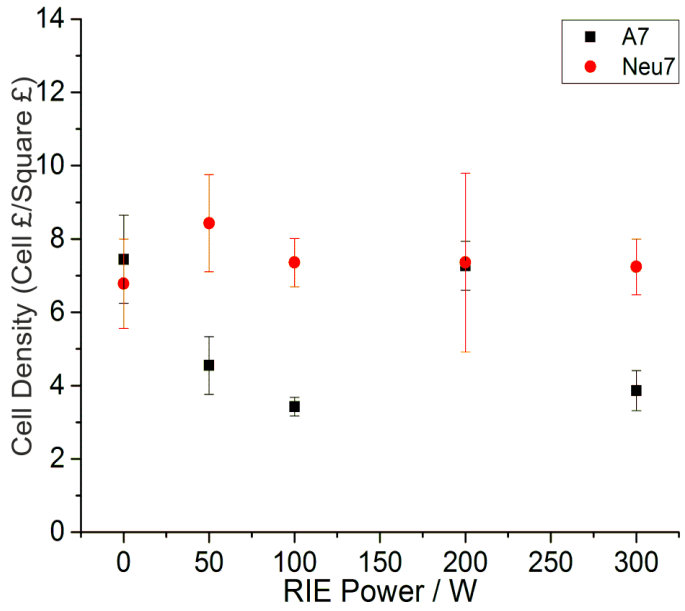

Figure 23 The A7 and Neu7 cell density (mean ± SD) from 3 different SU8 chips for different RIE powers.

difference in Neu7 cell densities. Taken together, this data suggests 0 W and 200 W are the most desirable degrees of roughness for SU8.

Chapter 5: Discussion

The aim of this study was to find the degree of roughness at which both impedance and compatibility were at their optimal, that is identify the range where compromises can be made towards choosing electrodes for stimulation, recording or both. Whilst, as shown in table 4, we did not find any overlap between degrees, we did succeed in finding the optimal degree of roughness for each condition. Explanations for our findings will now be discussed.

Table 4 The most desirable degrees of roughness in each scenario.

	Impedance (initial)	CSCc	CSCa	Biofouling	Biocompatibility
PBS	No sig. diff.	50, 75 W	50 W		
aCSF	0, 200 W	50 W	50, 75 W	50, 100 W	
RIPA				250 W	
Au					25, 100 W
SU8					0, 200 W

5.1 Electrode Impedance

Low electrode impedance is desirable for neural electrodes as it allows for sensitive detection of neural electrical activity *in-vivo*. Consistent with theory (section 2.1), electrode surface roughening has been used to lower impedance in literature (Bhandari et al. 2011; Seker et al. 2012; Koklu et al. 2016). Whilst studies have shown that roughened Au electrodes have lower impedance than non-roughened electrodes, they have only compared one degree of roughness to non-roughened (Chung et al. 2015; Koklu et al. 2016; Seker et al. 2010; Zhang et al. 2012). We measured the impedance across several degrees of roughness. Furthermore, in the studies listed, the electrode materials were roughened directly, as opposed to being layered over a pre-roughened surface like in our study. The objective here was to establish which degree of roughness had the lowest impedance. Based on previous literature, it was hypothesized that impedance would be inversely

proportional to roughness. In this study, impedance was measured in both phosphate buffered saline (PBS) and artificial cerebral spinal fluid (aCSF).

Unlike in the literature, we found impedance for all degrees of roughness (except 200 W) was greater than 0 W when measured in aCSF (figure 17A, section 4.2). In PBS, impedance was higher only for 25 and 150W compared to 0 W (figure 17 B, section 4.2). This discrepancy in the relationship between impedance and roughening, along with the difference between PBS and aCSF, is intriguing and is perhaps explained below.

5.1.1 Capacitance Reduction as a Factor for Impedance Increase

As described in section 2.1, capacitance is inversely proportional to impedance, so a decrease in capacitance will increase impedance. It is possible that with surface roughening, capacitance was decreased contributing to an increased impedance.

Electrode surface heterogeneities at the atomic scale have been shown to cause a decrease of capacitive behaviour, increasing impedance (Kerner 1998; Kerner & Pajkossy 2000; Bidola et al. 1994). Pajkossy (2005) argues that this type of capacitive decrease is due to two factors: 1) the locally conductive regions on the electrode - electrolyte interface allowing for ion adsorption 2) the varying affinity to adsorb onto the electrode surface amongst molecules. It is possible that Au deposited onto roughened SU8 has a large number of atomic scale surface features which reduce the capacitance at the electrode surface. This effect is characterised by consistently low phase angle over a large frequency range (1 Hz – 10 kHz) (Pajkossy 2005). Future tests to that may be done to provide evidence in support capacitance reduction from surface features will now be given.

Electrical impedance spectroscopy may be used. In electrochemical impedance spectroscopy, a sinusoidal AC voltage is generated between the counter and working electrodes and the current phase relative to the voltage is measured (figure 23). If the impedance is capacitive then the voltage changes fall behind the current changes. This is represented by a positive phase angle (as with figure 23, A and B). A phase shift of $+90^{o}$

therefore implies impedance is completely capacitive, whilst 0^{o} implies it is completely resistive. As a result, a surface with low capacitance behaviour would typically be characterised by a low positive phase angle. As shown in Appendix 2, figure 29, phase angle is lower for 100 W compared to 0 W throughout the frequency range, consistent with (Pajkossy 2005; Pajkossy 1991). Further analysis may be required to establish if a low capacitance is consistent with all roughened electrodes involving circuit modelling.

Circuit modelling involves the fitting of computer models of different theoretical circuit designs to impedance data over a range of frequencies. Different theoretical circuits would result in different phase responses for impedances measured over a frequency range (figure 24). In electrical impedance spectroscopy, phase response is presented by plotting real impedance against imaginary (figure 24C). Having a model that fits the data allows you to calculate the capacitive and resistive elements from it. Circuit modelling is the best way to accurately estimate capacitance and is the next step towards understanding capacitive change with roughness.

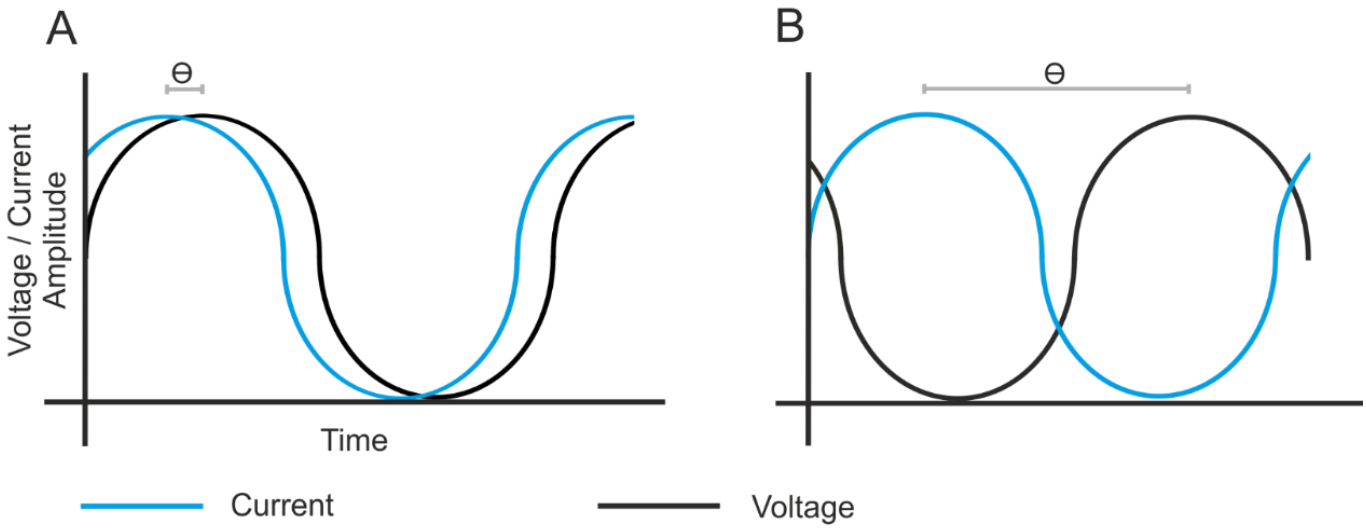

Figure 26 Diagram demonstrating how phase shift is calculated. Phase angle (Θ) between a sinusoidal AC voltage and current is calculated from phase shift between the two. Figure A shows a low phase angle implying mostly resistive impedance. B is a high phase angle implying mostly capacitive.

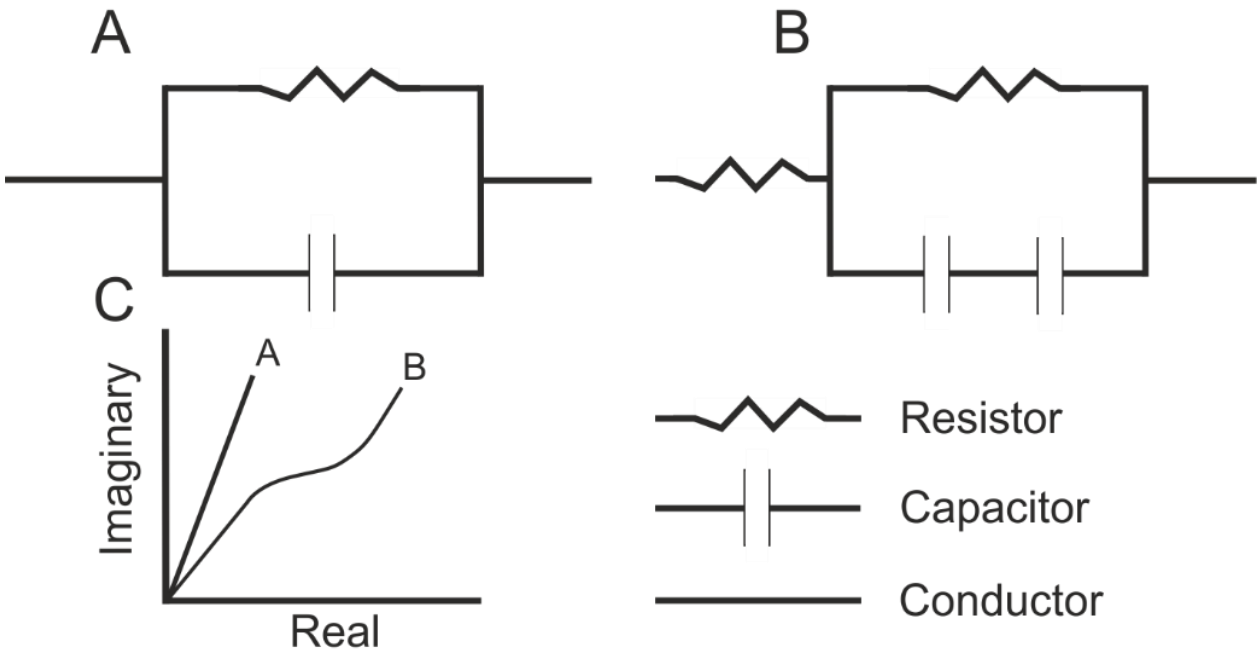

Figure 27 Example circuit models and their phase response. A and B are example circuit models. C is an example of how the phase response is displayed (Nyquist plot), including the phase response for the circuits A and B. The magnitude of the imaginary impedance is plotted against the magnitude of the real impedance (see section 2.1) over a limited range of frequencies.

Flame annealing is another way to provide evidence for capacitance reduction. Flame annealing is a process where the surface of the electrode is heated to below the melting point, leaving roughness unchanged on a scale detectable by a scanning electron microscope (Kerner & Pajkossy 2000). It has been shown to reduce capacitance dispersal on Au electrodes as it removes surface energetic heterogeneities (Kerner 1998). An increased capacitance after annealing would therefore be evidence suggesting atomic heterogeneities are the cause of impedance increase.

5.1.2 Impedance was Greater in aCSF

Impedance was higher in aCSF compared to PBS (figure 17, A and B, section 4.2). It is likely the impedance difference between aCSF and PBS is partly due to glucose (not in PBS – Table 1), which has been shown to increase impedance previously when added independently into solution (Tura et al. 2007; Park et al. 2003). This could be confirmed by repeating the impedance measurements in aCSF without glucose.

5.1.3 No Correlation between Roughness and Impedance

Correlations between Ra and impedance were conducted to see if impedance decreased with roughness. As shown in figures 17 C and D (section 4.2), there was no correlation when using either aCSF or PBS as electrolyte. It is possible that the size of the roughened electrode surface features were not large enough to increase capacitance as a result of being smaller than the Debye length. The Debye length (or radius) is a measure of a charge carrier's net electrostatic screening effect in solution. It is the distance from the atomic nucleus where the electric potential decreases by 1/e, where e is the charge of one proton (Debye 1936). If surface features are smaller than the Debye length of the ions in the solution, then capacitance increase is smaller as a result. If the features are small enough, then there is no measurable increase (Daikhin et al. 1996; Daikhin et al. 1997).

The Debye length was calculated using the concentrations given in table 2 at 18 ± 5^{o}C for aCSF and PBS using an online Debye length calculator (Kocherbitov 2015). The temperature was measured in the electrolyte during measurements to account for any heat generated from the electrochemical reactions. It was the same for aCSF and PBS, though it should be noted that temperature was only measured once for each on the same day. We have calculated Debye length at 18 ± 5^{o}C as an approximation of the effects of lab temperature fluctuation. Permittivity is a factor in Debye length and is discussed in more detail in sections 5.2.5 and 4.4.1. A relative permittivity of 80 was used for PBS (Zheng et al. 2013) and 84 was used for aCSF. A relative permittivity value of CSF was used for aCSF as we were unable to find one. As our aCSF composition was similar to CSF in literature, we believe this to be a reasonable approximation (Michel et al. 2016). Debye length was 0.29 ± 0.01 nm for aCSF and 0.8 ± 0.03 nm for PBS. However as shown in figure 15 (section 4.1), there are an increased amount of surface features greater than 2.5 nm in size with increasing RIE (reactive ion etch) powers. This suggests capacitance should also increase, thus decreasing impedance. The fact there is no correlation between roughness and impedance implies there is some other factor reducing capacitance. As discussed in section

5.1.2, we believe atomic scale surface heterogeneities may be a factor. With our data, and without further experimentation to confirm this theory, it is uncertain what other factors may have contributed.

5.2 Charge Storage Capacity

Charge storage capacity (CSC) is a measure of the maximal amount of charge that can be stored at the electrode surface before hydrolysis (García-Gabaldón et al. 2011). A high CSC is desirable for the stimulation of neural electrical activity *in-vivo*. CSC was measured using cyclic voltammetry to understand our electrodes potential as stimulating electrodes. CSC is divided into anodic (CSCa) and cathodic (CSCc). CSCa is a measure of how much negative charge can be stored at the electrode surface, whilst CSCc is a measure of how much positive charge can be stored. As with impedance, measurements were conducted using both PBS and aCSF as electrolyte. Based on previous literature, it was hypothesized that both CSCa and CSCc should increase with roughness (see section 2.2).

50 W was the only degree of roughness to increase CSCc in both PBS and aCSF. There was no change between degrees of roughness in CSCa when measured in aCSF. In PBS, 50 W CSCa was significantly larger than all degrees of roughness, and 75 W significantly larger than all except 0, 25 and 50 W. In both PBS and aCSF, correlations with both CSCa and CSCc against roughness had a very weak negative trend.

5.2.1 50 W Has the Largest CSCc in PBS and aCSF

As discussed in section 2.2, greater electrode surface areas are expected to have greater amounts of charge passing to/through the electrode-electrolyte interface. It is therefore surprising that the degrees of roughness with the highest CSC (50 and 75 W; figures 18 & 19, section 4.3) are not the highest degrees of roughness. To understand what may have caused this, knowledge of the type of charge injection mechanisms occurring is required. Inspection of the voltammogram (cyclic voltammetry scan) gives insight into what kind of charge injection mechanisms are occurring over a given voltage range. Explanations of the

results will now be given in reference to voltammogram shape. A brief explanation of how to interpret voltammogram data is given in Appendix 3.

50 W had the largest CSCc in both PBS and aCSF and, as shown in figure 16 (section 4.1), 50 W has the lowest degree of roughness. This conflicts with theory that suggests a low degree of roughness will have a small CSC (Aurian-Blajeni et al. 1987). It is uncertain why this is, though one possible explanation could be linked with surface feature shape. Different shaped surface features will give rise to different Au crystalline structures. The atomic scale surface structure of single crystalline Au has been shown to affect faradaic current amplitude, suggesting the surface structure of 50 W may result in the greatest rate of faradaic reactions (Kolb & Schneider 1986; Hamelin & Martins 1996). In line with this, previous literature theorised 'jagged' surface features decrease capacitance whilst increasing faradaic current (Zhao et al. 1999; Thomas 2012). Ionic species capable of undergoing faradaic reactions at the electrode surface are screened by the double layer. However, jagged surface features cause a break in the double layer, allowing faradaic reactions to occur. Admittedly, this effect has been reported on higher degrees of roughness (Zhao et al. 1999; Thomas 2012). However, it is possible that 50 W had sufficient jaggedness to measurably increase faradaic current.

As explained in Appendix 3, faradaic currents are typically characterised by a peak in the voltammogram. As shown in figure 30 (Appendix 3), current increase commonly continued to the end of the scan with 50 W instead of peaking. An explanation of the cause of this provides further information about the electrode surface so it is worth briefly discussing.

5.2.2 Unconventional Faradaic Peaks Explained by Edge Effect

Electrodes are commonly fabricated so that they rise above the level of the surrounding probe, exposing a surrounding edge to the solution (figure 25). Charge is able to build up / pass through the edge of the electrode. In microelectrodes, the edge is proportionately larger than macroelectrodes (figures 25 and B). This allows a proportionately larger amount of

current to build up at / pass through microelectrodes surface in comparison to macroelectrodes. The edge effect is a phenomenon where ionic diffusion towards the edge of microelectrodes reduces the diffusion limitations that normally cause the peaks shown in figure 25 C (Oldham 1981; Brownson & Banks 2014). The microelectrode's proportionately larger edge allows for a more efficient diffusion of charge towards/away from the electrode, resulting in a sigmoidal voltammogram (as shown in figure 25 D). The diffusion is less efficient in macroelectrodes since the diffusion at the edge is negligible in comparison to the face of the electrode. A voltage window only large enough to incorporate the linear region of the sigmoidal shape would explain the linearity seen in Appendix 3 figures 31 A and B.

As described in section 3.2.2, it should be noted that the edge of our electrodes are covered by an SU8 passivation layer. However the edge effect is also seen with domed electrodes

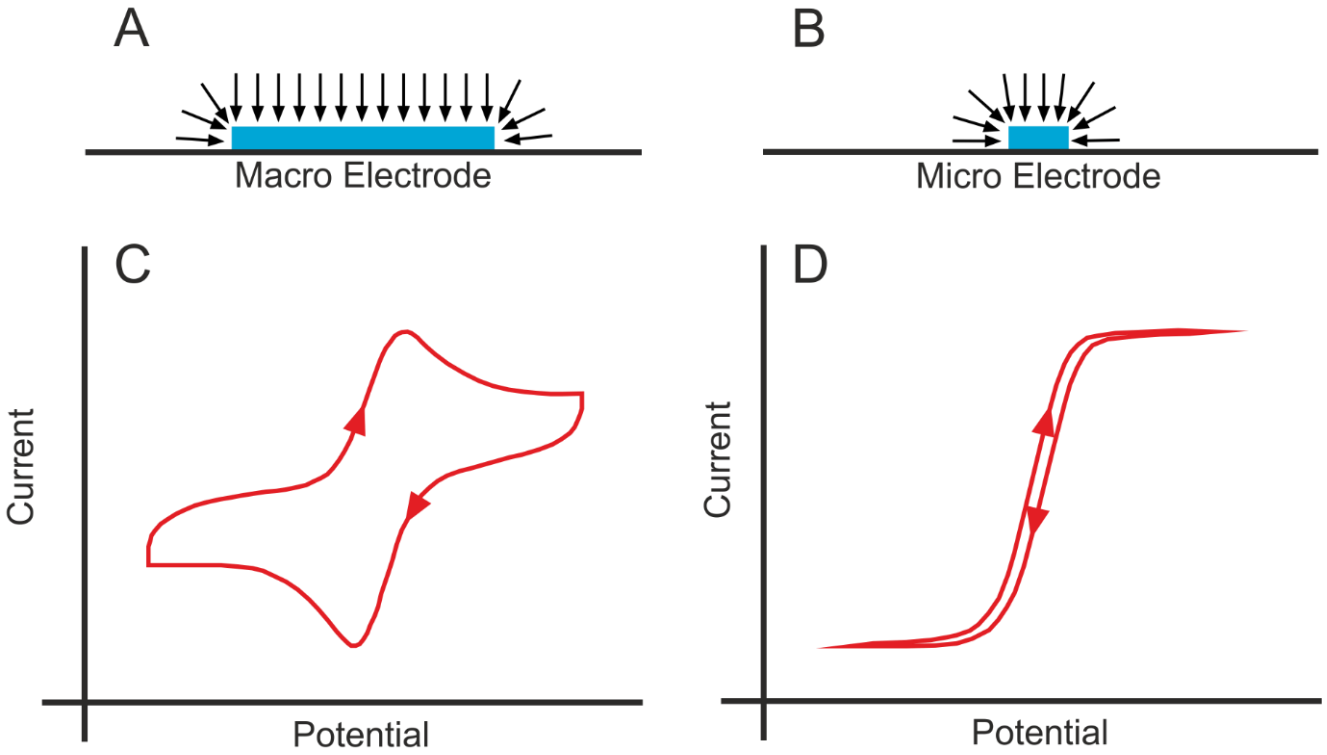

Figure 28 Edge effect. A and B illustrate the proportionate difference between diffusion at the edge vs the face of the electrode with a macroelectrode (A) vs a microelectrode (B). C and D are example voltammograms showing faradaic current occurring from edge effect at a macroelectrode (C) vs a microelectrode (D). Note the faradaic current peaks in C which do not exist in D due to a proportionately higher diffusion at the edge of the microelectrode compared to the macroelectrode. Triangles denote scan direction.

which would explain our results (Oldham & Zoski 1988). Further imaging analysis over a larger region of the electrode would however be required to confirm a dome shape.

5.2.3 50 and 75 W CSCa was Greater in PBS but not in aCSF

The fact that 50 and 75 W had significantly higher CSCa in PBS but not in aCSF begs two questions 1) why were 50 and 75 W the highest as opposed to higher degrees of roughness and 2) why was this not seen in aCSF? First, high CSCa for both 50 and 75 W seen in PBS appeared to be due primarily to faradaic currents (as with Appendix 3, figure 31). It is uncertain why these currents are so much larger with just 50 and 75 W, though it is possibly due to a combination of favourable Au polycrystalline surface structures (Kolb & Schneider 1986; Hamelin & Martins 1996) and increased current flow from jagged edges (Zhao et al. 1999; Thomas 2012), as discussed in section 5.2.2.

Second, different ionic species undergo redox reactions at different potentials (Rodríguez et al. 2000). It is therefore likely that the difference between CSCa in aCSF and PBS is due to interactions from different electrolyte species. However it is not possible to differentiate redox peaks due to the edge effect (section 5.2.2). The next step to understanding the role of different ions in creating these faradaic currents would be cyclic voltammetry in PBS with the removal of different ionic species. To better understand the faradaic peak current potential, electrodes with larger surface areas would be required to eliminate the edge effect.

5.2.4 Higher RIE Powers Had Minimal CSC

As shown in Appendix 4, figure 32 A, there was often an extremely low (< 20 pA) current during cyclic voltammetry for 150, 200 and 250 W. This occurred in both PBS and aCSF, though more commonly in aCSF. This is the reason 150, 200 and 250 W have the lowest CSC in aCSF. Due to this, correlations for both CSCc and CSCa against roughness showed a negative trend (figures 18 C-E and 19 C-F, section 4.3). It is uncertain what may have caused CSC to be so low for these electrode arrays. An obvious answer would be an insulating layer on the electrode surface. However, for a layer to produce so little current

during cyclic voltammetry, it would have to cause sufficient charge separation from the solution to eliminate capacitance (Thomas 2012). To test this, impedance was measured immediately after cyclic voltammetry scans. As shown in Appendix 4, figure 32 B, impedance at smaller frequencies (< 10 Hz) was lower than another electrode with a larger CSC, suggesting current was unaffected at frequencies greater than 1 Hz. However, it is possible current could be affected at frequencies less than 1 Hz. This could be tested by increasing cyclic voltammetry scan rate. Alternatively, the low CSC may be due to a poor connection between the Au wire bonding and the electrode array. Poorer connections may be found with higher degrees of roughness and only allow for current in the range required for impedance spectroscopy. This could be tested by comparing current increase to an AC voltage of increasing amplitude with an electrode array with a larger CSC. An upper limit in the current at the working electrode would suggest bonding issues. This was not done to protect the electrodes from corrosion.

It is possible permittivity is also a factor. Permittivity is the resistive force experienced when creating a flux of charge towards a dielectric, meaning a higher permittivity equates to less electric flux (see section 5.4.1). Permittivity is marginally higher in aCSF (84; Michel et al., 2016) than PBS (80; Zheng et al., 2013), which could contribute to low CSC was seen more in aCSF.

5.2.5 CSC is Greater in aCSF than PBS

As shown in figures 18 A and B and 19 A and B, CSC was higher in aCSF than PBS. As explained in Appendix 3 (figure 30 A), predominately capacitive CVs are recognisable by their rectangular like shape. There generally appeared to be a larger capacitance for CVs measured in aCSF. Unlike with double layer capacitance, psuedocapacitance voltammograms deviate from the rectangle form due to redox peaks connected with kinetic charging processes (Frackowiak & Beguin 2001). An example of this is highlighted in Appendix 3, figure 31). As psuedocapacitance amplitude differs with ionic species, voltammetry with each aCSF species in solution individually is required to understand their

individual roles pseudocapacitance. Since aCSF and PBS give different results, it is worth discussing the use of each of them as a model.

5.3 aCSF May Be a Superior Electrolyte Compared to PBS

PBS is typically used as an electrolyte for electrode measurements as it allows for comparison with other studies. aCSF contains the same ionic species as cerebral spinal fluid, making it a more biologically accurate model (Michel et al. 2016). As shown in table 1, PBS contains several different ionic species, making it less biologically accurate. Unsurprisingly, the two provide different results when used as electrolyte (as discussed in sections 5.1.3, 5.2.2 and 5.2.6). The point of measuring electrode performance *in-vitro* is to understand how the electrodes may perform *in-vivo*, meaning an accurate model of the *in-vivo* environment is desirable. Whilst aCSF has been used as an electrolyte to model *in-vivo* electrode use previously (Vahidpour et al. 2016), to the authors knowledge it has not been compared with PBS for its accuracy in modelling *in-vivo*. We suggest that this comparison should be done as it seems likely aCSF may provide a more accurate model.

5.4 Impedance Change due to protein adhesion

Protein adhesion at the electrode surface, or 'biofouling', is thought to increase electrode impedance *in-vivo*. The difference in impedance was found by comparing impedance before and after incubation with protein solution for different degrees of roughness. Publications have previously only used a single protein to model biofouling *in-vitro* (Patel et al. 2013; Moulton et al. 2004; Sommakia et al. 2014; Sommakia et al. 2009). The objective was to find which degree of roughness underwent the smallest impedance increase from biofouling. We tested this using a multiprotein model which is more biologically accurate than single protein models previously used. It consisted of a tissue homogenate dissolved in either RIPA (radioimmunoprecipitation assay) buffer or aCSF. The hypothesis was that impedance increase would be greater for larger degrees of roughness. Interestingly, we found that impedance *decreased* following incubation with aCSF protein solution for all degrees of roughness except 0 W (figure 20 B, section 4.4). With RIPA protein solution, impedance

decreased for all degrees except 75 and 150 W (figure 20 A, section 4.4). With aCSF protein solution, 25, 50, 75 and 100 W had a significantly smaller impedance increase than 0 W, whilst no difference between degrees of roughness from RIPA protein solution. To understand why impedance decreased, impedance theory must be expanded. As mentioned (section 5.1.1), impedance consists of both capacitive and resistive elements. As it is possible that protein adhesion affects both of these, this discussion will now look at them individually, starting capacitance.

5.4.1 Impedance Decrease - Capacitance

In-vivo studies suggested impedance increase from biofouling was due purely to a rise in resistance (Malaga et al. 2016; Otto et al. 2006; Johnson et al. 2005). However contrary to this, previous *in-vitro* studies have reported an capacitance increase accompanying an increase in resistance following protein adhesion (Moulton et al. 2004; Sommakia et al. 2014). Capacitance may have also increased in this study since an increased phase angle was often associated with a reduction in impedance (an example of this is given in Appendix 5, figure 33). Capacitance increase may be possible because proteins commonly become charged in solution (Ohno et al. 2009), resulting in a build-up of charged protein molecules at the electrode surface. Double layer capacitance formed by a mixture of proteins and ions may be greater than if formed purely by ions due to an increase in permittivity. As mentioned, permittivity is a measure of the resistance encountered when forming an electric field. When creating an electrochemical double layer, a solution with larger sized charged particles will have a higher permittivity as it will require a larger amount of energy to move the particles close to the electrode. This also means there is a greater amount of energy stored at the electrode. Protein molecules are far larger than the ions and generally have a much lower charge density (Park et al. 1992). This means a greater amount of charge is required pull protein molecules through solution in comparison to the smaller, more charge dense ions, resulting in an increased permittivity. Double layer capacitance is a function of permittivity and, as mentioned, the electrode surface area. This relationship is given in

equation 1 where C is capacitance, ε_r is the relative permittivity, ε_0 the vacuum permittivity ($8.9E^{-12}$ F/m), A is the area of the electrode and d is the distance between the electrode surface and the centre of the ion layer.

$$\mathbf{C = \frac{\varepsilon_0 \varepsilon_r A}{d}} \qquad \textbf{Equation 1}$$

It is important to note that since studies have reported an increase in capacitance *in-vitro* (Moulton et al. 2004; Sommakia et al. 2014), *in-vivo* models suggestions of biofouling causing an increased impedance purely from an increased resistance may not be accurate since the capacitive increase caused by biofouling are not accounted for. This discrepancy has two potential causes: First, the *in-vivo* studies circuit modelling estimations of the cause of impedance increase were inaccurate. Second, the *in-vitro* studies have not accurately modelled the *in-vivo* environment.

5.4.2 Impedance Decrease - Resistance

Whilst other studies have found increased capacitance, they have also found an increased solution resistance that has the net effect of raising impedance (Moulton et al. 2004; Sommakia et al. 2014). As mentioned, previous *in-vitro* models have only used a single type of protein for each measurement (Moulton et al. 2004; Sommakia et al. 2014; Patel et al. 2013; Sommakia et al. 2009). Naturally, this limits the types of interactions occurring between the electrode and electrolyte proteins. If capacitance increase from protein adhesion occurred alongside a proportionately smaller resistive increase, the net effect would be impedance decrease. Examples of this have been reported previously: Martic et al. (2013) showed that copper ions binding to tau protein immobilized on Au electrodes enabled the tau protein to take part in reduction/oxidations reactions, increasing the flow of charge between the electrode/electrolyte. Similar effects have also been shown following the binding of amyloid-beta oligomers and cellular prion protein (Rushworth et al. 2014) and following exposure of silicon electrodes to tetracycline (Zhang et al. 2012). If such

interactions exist, it seems reasonable to speculate that other protein-electrode, or protein-protein-electrode, interactions that ameliorate the increase in the solution resistance caused by protein adhesion may have occurred here. Considered alongside an increase in capacitance, this could explain why there was a decrease in impedance following incubation with protein solution.

5.4.3 The Effect of Biofouling Reduced with Roughness

Impedance decrease from biofouling was negatively correlated with roughness linearly for RIPA protein solution (figure 20 D, section 4.4) and in a sigmoidal fashion for aCSF protein solution (figure 20 F, section 4.4). It is possible this is due to a decrease in capacitance. Protein has been found to adhere in greater quantities to roughened surfaces (Salakhutdinov et al. 2008). If we assume this is the case here, then an increase in the amount of protein at the electrode surface is causing either the decreased capacitance or increased resistance. As shown in equation 1 (section 5.4.1), an increase in the distance between the surface of the electrode and the centre of the electrochemical double layer would lower capacitance. Since roughened electrodes have an increased surface area, an increased amount of protein adhesion is possible if you assume the protein layer is of

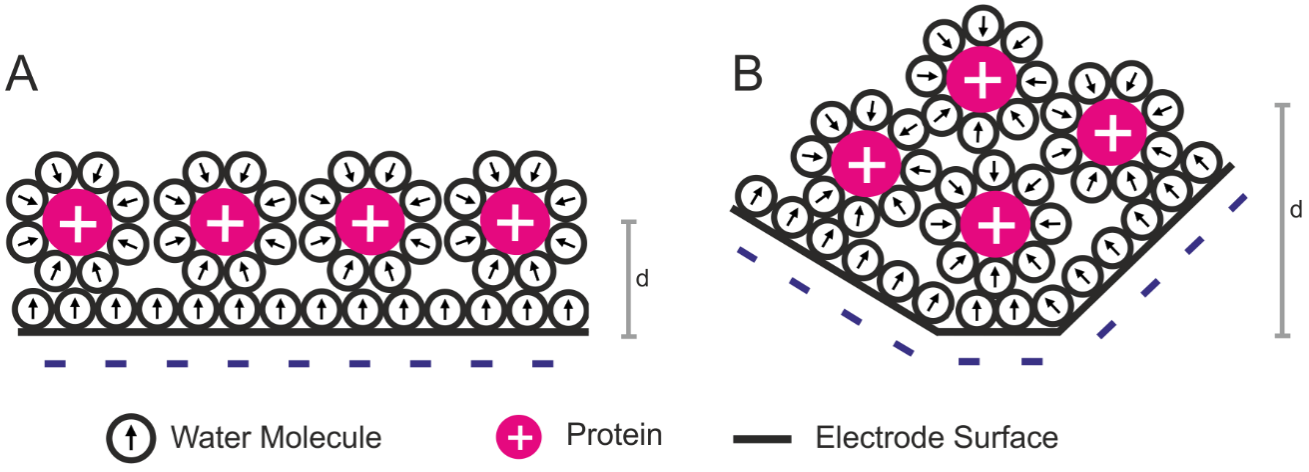

Figure 29 Difference between the distance (d) between electrode surface and the centre of the electrochemical double layer on smooth electrode surface vs rough. A is smooth and B is rough. Protein molecules between the surface features on rough electrode surfaces have the effect of thickening the electrochemical double layer.

uniform thickness. This would not increase electrode-double layer distance. However as shown in figure 26, protein may instead form a layer of uneven thickness if it fills pores on the roughened surface. This would increase the electrode surface-double layer distance, reducing capacitance. Increase protein build-up at the surface would however also increase permittivity. In figure 20F (section 4.4) there appears to be a saturation in the correlation. This may be due to a balancing in the effects of increased distance and permittivity.

5.4.4 Greater Impedance Reduction from aCSF Protein Solution

There are a larger amount of data points (including error bars) that have had a negative change in impedance following incubation with aCSF protein solution in comparison to RIPA (figures 20 B and A, respectively, section 4.4). This may be due to the pH of the solutions. A protein's isoelectric point is the pH value at which the mean charge of the protein molecule is zero. pH is therefore important when considering changes in both capacitance and resistance from protein adhesion: Capacitance would be altered as a change in the amount of charged molecules will affect the size of the double layer formed. Resistance would be altered as a change in the amount of charged molecules will affect the way in which proteins interact with each other and the electrode. In line with this, Chen et al. (2005) showed that faradaic impedance following incubation with IgG was pH dependant, as well as all the studies referenced that reported a decrease in solution resistance (Martic et al. 2013; Rushworth et al. 2014; Zhang et al. 2012). These emphasize the importance of using a biologically accurate pH when modelling biofouling. Extracellular pH has previously been reported to be ~ 7.3 (Chesler 2008; Cragg et al. 1977). As aCSF pH is closer to *in-vivo* than RIPA (7.83 vs 8.08, respectively), aCSF is more likely to provide a more accurate model. This point will now be expanded upon.

5.4.5 aCSF Protein Solution is a Better Model Than RIPA Buffer Solution?

aCSF and RIPA buffer protein solutions were designed to model the *in-vivo* environment following protein release after cell lysis. However unlike aCSF, RIPA contains ingredients

such as sodium deoxycholate and nonyl phenoxypolyethoxylethanol which are not found in the brain or spinal cord making it a less accurate model. As well as not being found in the brain or spinal cord, deoxycholate and nonyl phenoxypolyethoxylethanol are lysing agents which can denature proteins (Ngoka 2008). Interestingly, we found that within group to out of group variance ratio was larger for impedance change following incubation with RIPA buffer protein solution compared to aCSF protein solution, suggesting RIPA has less consistent results. Protein denaturation (i.e. disruption and/or destruction of structure) may possibly have contributed to this. The presence of denatured proteins would increase the range of protein interactions.

Interestingly, as shown in figure 20 (section 4.4), there are a larger amount of data points (including error bars) below the 0 MΩ line with aCSF protein solution in comparison to RIPA. This suggests that incubation with aCSF protein solution lowers impedance more than RIPA protein solution. This may partly be explained by diffusion. Following electrode incubation with RIPA solution, the electrode array was submerged in aCSF with the RIPA buffer solution still on the surface (as in figure 27). Upon submersion, a diffusion gradient between the protein solution and electrolyte would form. As there is a greater difference between RIPA proteins solution and aCSF compared with aCSF protein solution and aCSF, there would also be a greater diffusion gradient (figure 27). A larger diffusion would result in a larger migration of protein away from the electrode surface, thus reducing electrode – protein

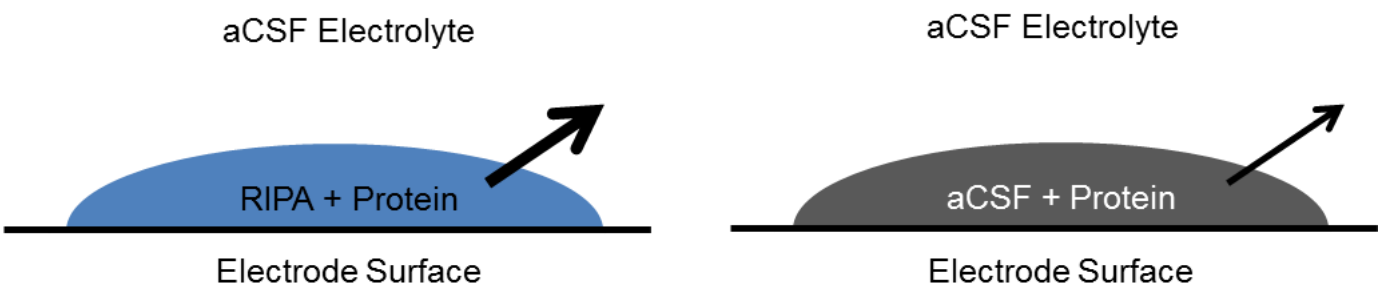

Figure 30 Diffusion between aCSF electrolyte and protein solution on the electrode surface. Protein solution is on the electrode surface as the electrode array is submerged in aCSF electrolyte, resulting in a diffusion gradient between the protein solution and electrolyte. There is a higher diffusion gradient between aCSF electrolyte and RIPA as shown by the arrows.

interaction in RIPA protein solution.

5.5 Biocompatibility

Electrode insertion into the brain and spinal cord causes the formation of an electrically insulating tissue known as glial scarring around the probe which is generally believed to be a primary cause of electrode failure (Kozai et al. 2014). Reducing glial scar formation - or improving biocompatibility - is therefore highly important for increasing the functional lifespan of electrodes *in-vivo*. One idea is to improve adhesion of non-pro-inflammatory cells (i.e. non-activated astrocytes), reducing glial scar formation. In an attempt to do this, we have tested surface roughening using an *in-vitro* model.

As discussed in section 2.3, it is desirable to create a probe that is more conducive to non-activated astrocyte survival than activated. To test if this was the case for roughened Au surfaces, astrocytes were cultured on roughened surfaces and cell density was measured for each degree of roughness. We have chosen Neu7 and A7 astrocytic cell lines to model activated and non-activated cells, respectively (Fidler et al. 1999; Elizabeth M Powell et al. 1997; Smith-Thomas et al. 1995). A comparatively high density of A7 and a low density of Neu7 was therefore desirable. The objective was to find the degree of roughness with highest A7 and lowest Neu7 density on both Au and SU8.

5.5.1 Findings

On Au, we found that 25 and 100 W had higher A7 cell densities than other degrees of roughness suggesting they were the most desirable for increasing biocompatibility (figure 21 A, section 4.5). Conversely, 200 and 300 W had higher Neu7 cell densities than other degrees suggesting they are the least desirable degree of roughness for increasing biocompatibility. There was no correlation between roughness and A7 density. A weak correlation (r^2 = 0.66, figure 21 D, section 4.5), between Neu7 and roughness suggests Neu7 density increases with roughness.

Unlike Au, on SU8 all degrees of roughness (except 200 W) had significantly lower A7 densities than 0 W (figure 22, section 4.5). There were no significant differences in Neu7 densities. This suggests roughening decreases biocompatibility on SU8. Cell density differs as varying amounts of cells fail to anchor to the Au or SU8 surface. The potential causes for these results will now be discussed.

5.5.2 Cell Density Varies, But Does Not Correlate, With Roughness

As discussed in section 2.4, cell binding is highly sensitive to surface feature shape, size and spacing. As also mentioned, Biggs et al. (2010) argue protrusions with a height and spacing > 70 nm, and widths < 70 nm are disruptive to cell binding, whilst protrusions with the opposite dimensions aid binding. It must be noted that many of the studies listed in Biggs et al. (2010) had surface features of consistent size and spacing. As shown in figure 15 (section 4.1) the surface features on each of our roughened Au surfaces consisted of a variety of sizes. In this case, it would seem that the degree of roughness most conducive to cell survival is the surface with the highest amount of feature sizes within the specified range. It is possible that by increasing the roughness, you increase the amount of surface features in the specified size range. However if this was the case, there would be a correlation between roughness and cell density. One explanation for this may be linked to how surface features form during RIE. As shown in figure 16 (section 4.1), increasing RIE power will etched the surface to increasing depth. As with literature, this resulted in the formation of increasingly large surface features (Oehrlein & Lee 1987; Oehrlein & Kurogi 1998). However as the material is etched, some surface features are also decreased in size. This means that whilst you are increasing surface roughness, you may not be increasing the amount of surface features within the optimal size range for cell binding. This would explain why there is not a consistent increase in the amount of cells binding with an increase in roughness. To confirm this would require obtaining a surface feature size range for each RIE power from the AFM data.

5.5.3 A7 Density is Lower than Neu7 on SU8

Cell density was measured on roughened SU8 surfaces. As shown in figure 5 B (section 3.2.2), the majority of the probe surface area is SU8. Improving cellular interactions with SU8, or any other passivation material, would therefore be a powerful tool in reducing gliosis. As with Au, the objective was to find the degree of roughness with the highest biocompatibility. We found that A7 cell densities were significantly lower for all degrees of roughness in comparison to 0 W (figure 22, section 4.5). This suggests that 0 W is the optimal degree of roughness. There was no significant difference for Neu7. Interestingly, unlike Au mean Neu7 cell densities were higher on SU8 than A7 for all degrees of roughness except 0 W. This suggests that roughening decreases biocompatibility on SU8. We suspect the difference between cell binding affinities on Au and SU8 are due to two reasons.

First, as described in section 3.2.3, Au surfaces were fabricated by plating Au onto a roughened SU8 surface. It is therefore uncertain how similar the surface morphology is between Au and SU8 chips of the same RIE power, though it is likely a smoothing effect occurs with Au plating (Tian et al. 2002). To clarify this, AFM imaging is required. Sadly it was not possible to image SU8 chip surfaces, so we are unable to compare them. This is also why no correlations between cell density and roughness were conducted.

Second, proteins have different binding affinities to different materials. There are many complex factors effecting protein adsorption affinity relating to surface properties including surface energy, intermolecular forces, hydrophobicity, and ionic or electrostatic interaction. These differ between SU8 and Au. For example, SU8 is more hydrophobic than Au (Xue et al. 2014). The difference in protein affinity will alter the formation of the extracellular matrix at the SU8 surface, thus altering cell adhesion.

5.5.4 Highest Neu7 and A7 Cell Densities are on Different RIE Powers

The fact that there were different optimal binding conditions for Neu7 and A7 implies there are factors related to the cell line affecting binding. Neu7 was chosen to model activated astrocytes because it produces chondroitin sulphate proteoglycans such as NG2 and versican (Fidler et al. 1999). These block neurite extension and form part of the extracellular matrix (Smith-Thomas et al. 1995; Fidler et al. 1999). They may also change Neu7 binding affinity to different Au degrees of roughness by altering extracellular matrix conformation.

Proteoglycans fill the majority of the extracellular space and aid cell binding as well as provide force resistive properties (Schaefer & Schaefer 2010). As well as proteoglycans, the extracellular matrix also consists of fibrous proteins such as fibrinogen and collagen which bind to cells and provide structural support (Frantz et al. 2010). The addition of different proteoglycan or fibrous protein species into the extracellular matrix will alter extracellular matrix structure (Wight 2002; Frantz et al. 2010). Versican expression is high in the cervix during pregnancy but is known to drop dramatically during involution, implying its presence creates a more loosely organised extracellular matrix to accommodate developmental events (Westergren-Thorsson et al. 1998). Thus, it seems likely that the addition of versican will change the interaction between the roughened Au surface and extracellular matrix components. This could explain the difference between A7 and Neu7 densities.

Chapter 6: Conclusions and Future Works

6.1 Concluding Remarks

Chronic *in-vivo* electrode function requires the electrode to be able to surpass the effects of both biofouling and biocompatibility, either of which may cause electrode failure. It is therefore essential to investigate the effects of both of these whilst testing extra cellular electrodes *in-vitro*. This is the first study to compare electrode roughening's ability to combat *both* glial scarring and biofouling in the same study. We also compared electrode function between degrees of roughness. The aim of this study was to find the roughness at which impedance, CSC, biofouling and biocompatibility were at their best.

We found that roughening increased impedance and only increased CSC for two degrees of roughness (50 and 75 W). As shown in table 4 (section 5), the most biocompatible degrees of roughness do not overlap with those most desirable for recording or stimulating. We suspect that our fabrication technique increased the amount of atomic scale surface heterogeneities which reduced capacitance. This appeared to supersede the effects of roughening in the range of roughness fabricated. As such, we conclude we did not have the optimal size range for roughening with our fabrication method.

This was the first study to use a multiprotein biofouling model. This likely to be far more biologically accurate than the single protein models commonly used in literature. Our results suggest that a combination of increased capacitance and protein-protein interactions may be responsible for lowering impedance following biofouling. This is intriguing as it may be cause to re-evaluate the cause of impedance increase from biofouling.

This was the first study to compare the electrolytes aCSF and PBS. The choice of aCSF as an electrolyte was significant as it provided different results to the less biologically accurate, though more commonly used, PBS. We suggest *in-vivo* modelling accuracy of PBS and aCSF accuracy be compared.

6.2 Future Directions

As discussed above (sections 5.1.2 and 5.4.1), circuit modelling is required to understand the causes of impedance change. Using it to confirm whether a reduced capacitance is a leading factor for increasing impedance with roughness (section 5.1.2) is the next step. It will also be used to understand how our biofouling model changed both capacitance and resistance (sections 5.4.1 and 5.4.2).

Our finding that a mixture of proteins decrease impedance (figure 20, section 4.4) is in contradiction to findings in literature which suggest incubation with single protein species increases impedance (Newbold et al. 2010; Moulton et al. 2004; Di et al. 2011). To validate our findings, the experiment (as in section 3.6.2) should be redone using fibronectin, human serum albumin and immunoglobulin G as has been done in the literature. If we find similar results to the literature, it is likely the difference is due to protein-protein interactions as opposed to experimental conditions. This would strengthen our claims.

This study was the first to test the biocompatibility of a roughened passivation material. Polyimide is a widely used alternative passivation material (Fattahi et al. 2014). As discussed in section 5.5.4, ECM protein-probe surface interactions differ between materials. Roughened Polyimide will therefore have different biocompatibility to SU8. The biocompatibility of roughened Polyimide would be the next thing to be tested. A wider range of roughness should be used to find the degree with the maximal amount of surface features within the optimal size range.

Finally, PBS and aCSF's ability to model the *in-vivo* environment should be compared. The significant effects of biofouling occur during the first week - not hours - of insertion (Kozai et al. 2016). Therefore, comparison to electrode impedance during the first few hours of insertion *in-vivo* could be compared to both PBS and aCSF.

Appendix 1

Figure 28 is the BCA standard curve used to estimate the concentration of our RIPA protein mixture.

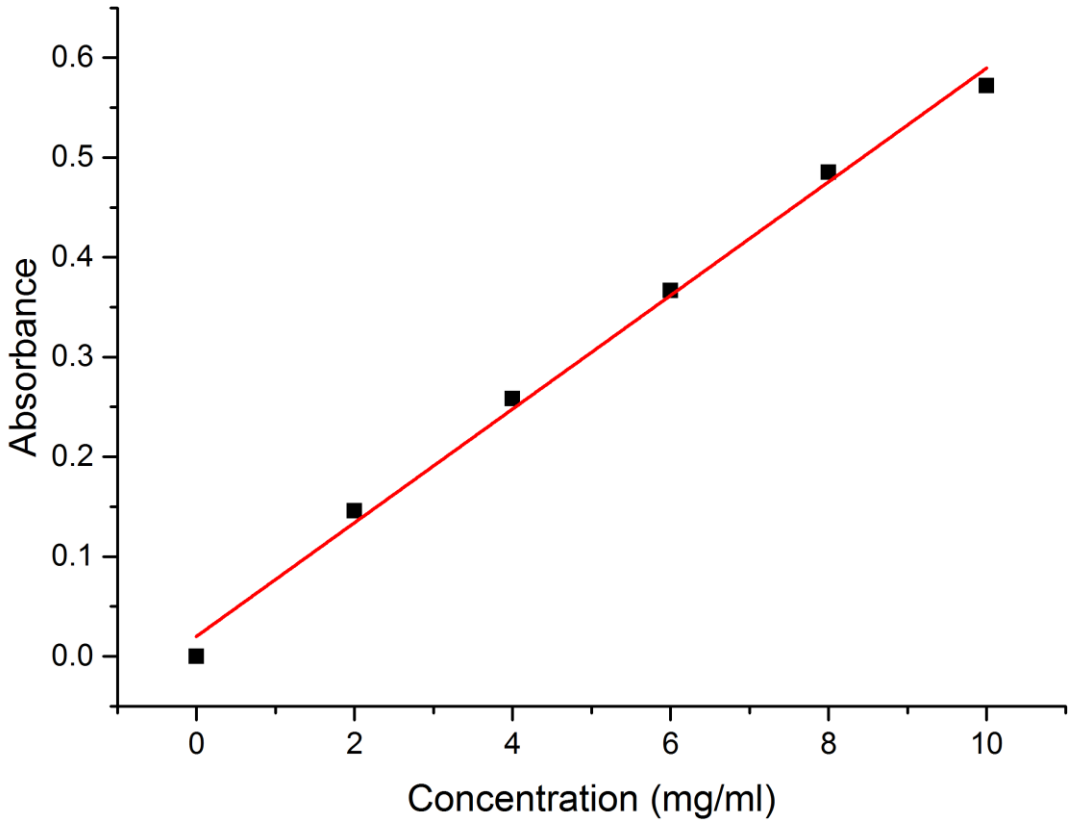

Figure 31 BCA standard curve generated from the absorbance of protein standards at 562 nm.

Appendix 2

Figure 29 is an example of how phase angle changes with different frequencies during electrochemical impedance spectroscopy. In electrochemical impedance spectroscopy, a sinusoidal AC voltage is applied over a broad range of frequencies between the counter and working electrode. Impedance is measured by the current and phase in response to this voltage. If the current at the working electrode is 90^{o} behind phase from the voltage, impedance is considered completely capacitive. A perfectly in phase (i.e. 0^{o}) current response would suggest an entirely resistive impedance. A low phase angle is therefore suggestive of capacitance dispersion. Capacitance dispersion occurring from monoatomic

surface inhomogeneity's is typically characterised by a flat line phase response at a low phase angle as with 100 W (Pajkossy 1997; Pajkossy 2005; Kerner & Pajkossy 2000). Note how impedance is higher for 100 W at 1 kHz.

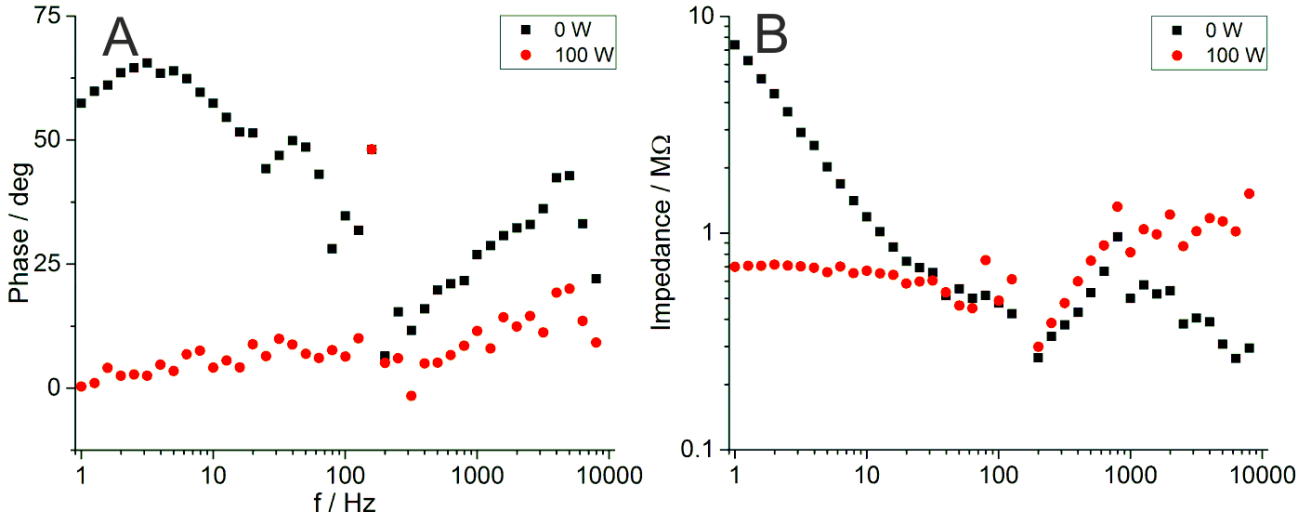

Figure 29 Example of how a decreased phase angle is associated with a larger impedance on roughened electrodes. A is the phase angle over a range of frequencies for both 0 and 100 W. B is the impedance for the same scan. Note the consistently low phase angle for 100 W is associated with a higher impedance.

Appendix 3

Figure 30 gives example voltammamograms showing the difference in CSC between 0 and 50 W. In the voltamammogram, the shape of the curve plotted allows you to identify different charge injection mechanisms by their characteristic form. A perfectly capacitive surface will have a rectangular shape characterised by horizontal cathodic and anodic phases. This is explained by equation 2 where I is current flowing to/away the capacitor, C is capacitance, V is voltage and t is time (Compton & Banks 2011).

$$I = C\frac{V}{t} \qquad \textbf{Equation 2}$$

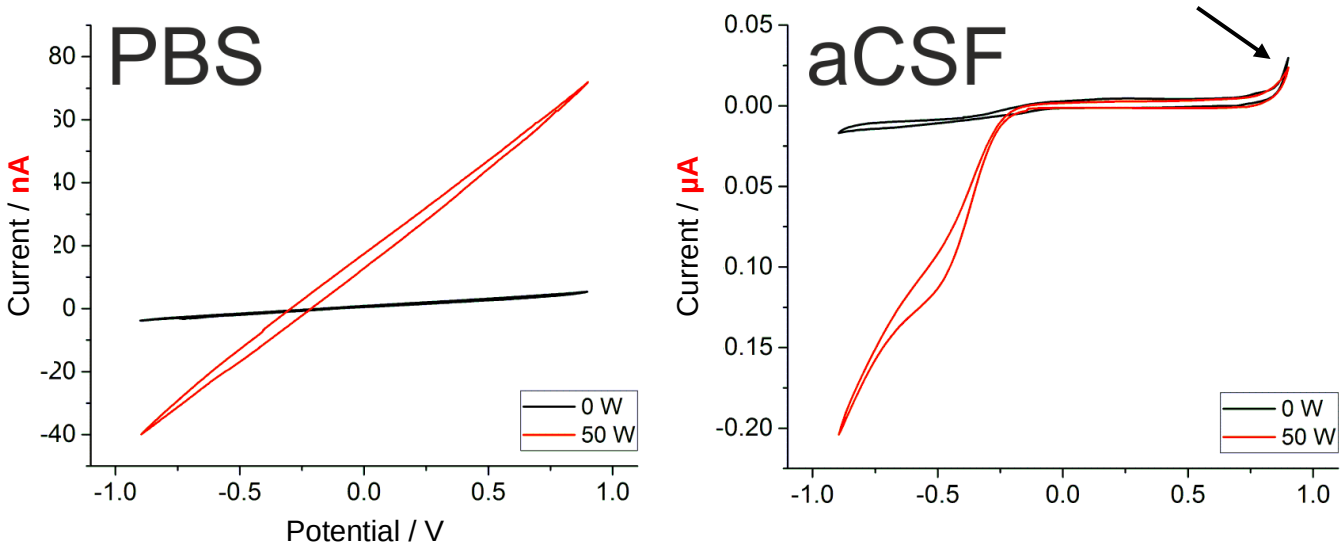

Figure 35 Example small and large voltammograms from 0 and 50 W respectively, recorded in PBS and aCSF. Arrow highlights faradaic peak typical of pseudocapcitance. Please note the **different y axis scales.**

This shows that for a constant scan rate (V/t), there is a constant current. Cyclic voltammetry scans between voltages in a triangular fashion, resulting in a near instantaneous change of current. An example of this is given in figure 31 A.

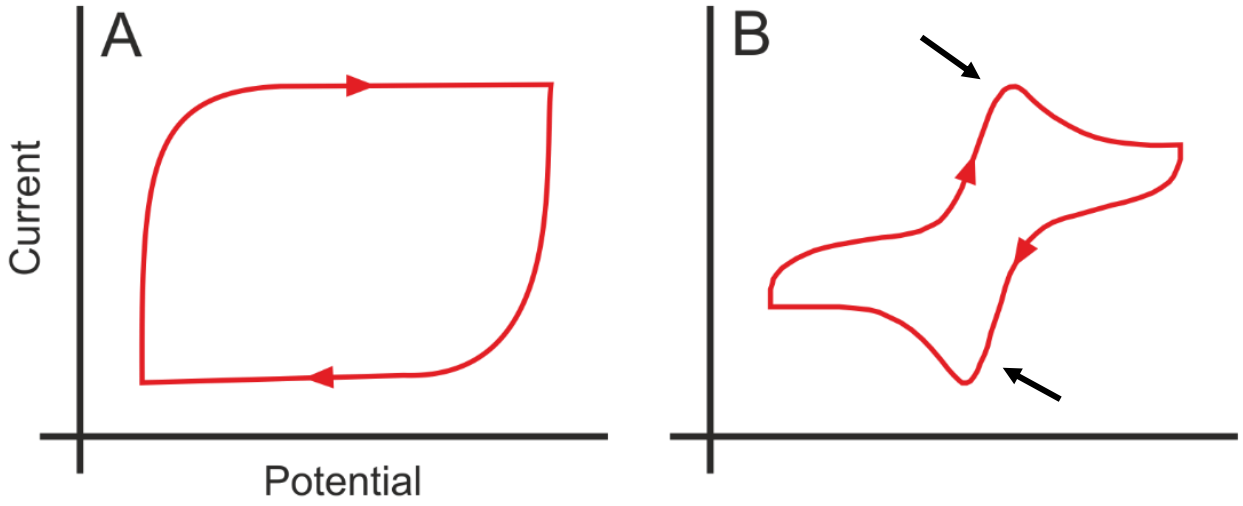

Figure 36 Example voltammograms displaying capacitive and faradaic charge injection mechanisms. A is a highly capacitive voltammogram. Note the constant current mid phase and sudden change with the change of voltage. Conversley, the peaks highlighted by the black arrows in B are examples of faradaic currents.

Faradaic charge injection is characterised by sudden peaks in current. The equilibrium potential is the potential where the rate of redox reactions are equal, and differs between reactions. If the rate of, for example, oxidation reactions is greater than reduction at the electrode surface, there will be a net movement of electrons into the electrode from solution, creating current. As the voltage moves further away from the equilibrium potential, a greater proportion of redox reactions will be either oxidation or reduction. This increases the amount of electrons flowing into the electrode as well as the amount of oxidised or reduced ions around the electrode surface. After a certain point, the current will drop as ions become less able to diffuse towards the electrode surface, resulting in a peak like in figure 31 B.

Appendix 4

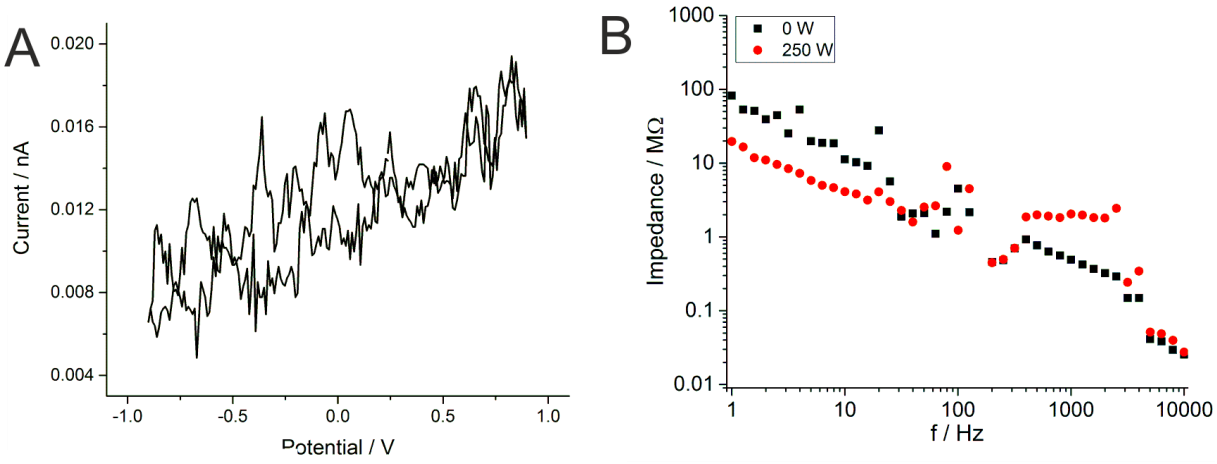

Figure 37 Example of extremely small voltammogram with corresponding impedance magnitude and phase. A is an example voltammogram with extremely small, noisey current. B is the impedance magnitude from the same electrode (250 W), measured immediately after A, compared with another electrode with a larger CSC.

Appendix 5

Figure 27 gives an example of an increased phase angle following incubation with proteins. This is associated with a decrease in impedance.

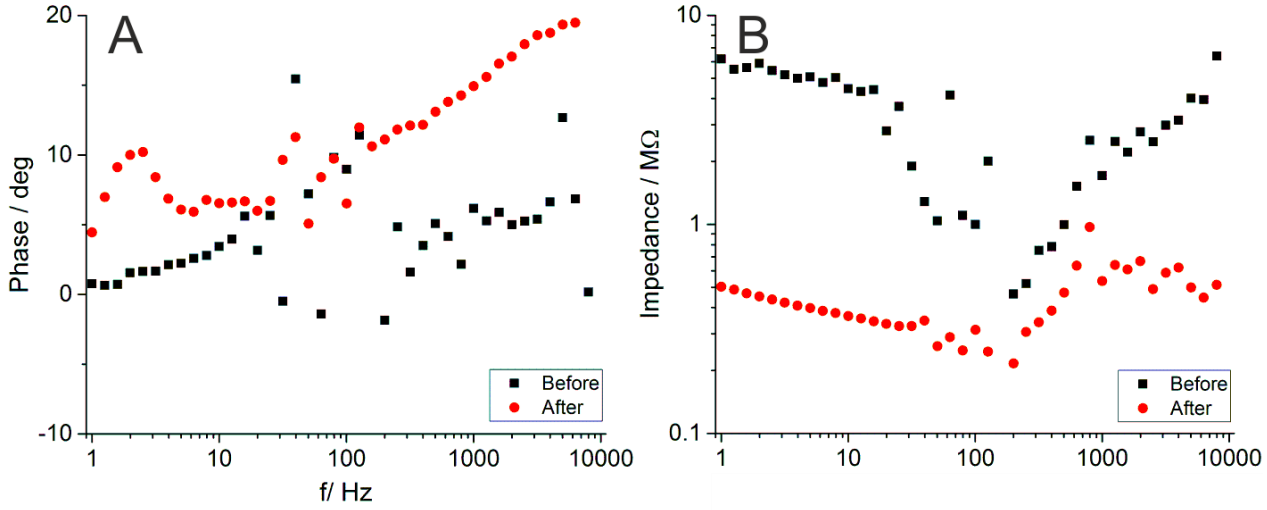

Figure 38 Example of how an increased phase angle is associated with lower impedance after incubation with protein solution. A is the phase angle for an electrode before and after incubation with protein solution. B is the corresponding impedance.

Bibliography

Alexander, C.K. & Sadiku, M.N.O., 2001. *Fundamentals of Electric Circuits* 3rd ed., New York: McGraw-Hill Higher Education.

Altuna, A. et al., 2013. SU-8 based microprobes for simultaneous neural depth recording and drug delivery in the brain. *Lab on a chip*, 13(7), pp.1422–30.

Altuna, A. et al., 2012. SU-8 based microprobes with integrated planar electrodes for enhanced neural depth recording. *Biosensors and Bioelectronics*.

Altuna, A., Berganzo, J. & Fernández, L.J., 2015. Polymer SU-8-Based Microprobes for Neural Recording and Drug Delivery. *Frontiers in Materials*, 2(June), pp.1–5.

Aurian-Blajeni, B., Kimball, A.G. & Robblee, L.S., 1987. Correlation Between Charge Storage Capacity and Morphology. *Journal of The Electrochemical Society*, pp.2637–2638.

Babcock, A. a. et al., 2003. Chemokine Expression by Glial Cells Directs Leukocytes to Sites of Axonal Injury in the CNS. *J. Neurosci.*, 23(21), pp.7922–7930.

Balaban, N.Q. et al., 2001. Force and focal adhesion assembly: a close relationship studied using elastic micropatterned substrates. *Nature cell biology*, 3(5), pp.466–472.

Barrese, J.C. et al., 2013. Failure mode analysis of silicon-based intracortical microelectrode arrays in non-human primates. *Journal of Neural Engineering*, 10(6), p.66014.

Bershadsky, A.D. et al., 2006. Assembly and mechanosensory function of focal adhesions: Experiments and models. *European Journal of Cell Biology*, 85(3-4), pp.165–173.

Bhandari, R., Negi, S. & Solzbacher, F., 2011. A novel surface modification method to achieve low impedance neural microelectrode arrays. *2011 16th International Solid-State Sensors, Actuators and Microsystems Conference, TRANSDUCERS'11*, pp.2196–2199.

Bidola, E.D., Bulhoes, L.O.S. & Rocha-Filho, R.C., 1994. Pt / HCl04 Interface CPE: Influence of Surface Roughness and Electrolyte Concentration. *Electrochimica Acta*, 39(5), pp.763–769.

Biggs, M.J.P., Richards, R.G. & Dalby, M.J., 2010. Nanotopographical modification: a regulator of cellular function through focal adhesions. *Nanomedicine: Nanotechnology, Biology, and Medicine*, 6(5), pp.619–633.

Biran, R., Martin, D.C. & Tresco, P.A., 2005. Neuronal cell loss accompanies the brain tissue response to chronically implanted silicon microelectrode arrays. *Experimental Neurology*, 195(1), pp.115–126.

Bjornsson, C.S. et al., 2006. Effects of insertion conditions on tissue strain and vascular damage during neuroprosthetic device insertion. *Journal of neural engineering*, 3(3), pp.196–207.

Boehler, C. et al., 2015. Iridium Oxide (IrOx) serves as adhesion promoter for conducting polymers on neural microelectrodes. *IEEE*, 49, pp.22–24.

Bosman, F.T. & Stamenkovic, I., 2003. Functional structure and composition of the extracellular matrix. *Journal of Pathology*, 200(4), pp.423–428.

Brownson, D.A.C. & Banks, C.E., 2014. *The Handbook of Graphene Electrochemistry* 1st ed., London: Springer.

Buffo, A., Rolando, C. & Ceruti, S., 2010. Astrocytes in the damaged brain: Molecular and cellular insights into their reactive response and healing potential. *Biochemical Pharmacology*, 79(2), pp.77–89.

Burridge, K., 1988. Focal Adhesions: Transmembrane Junctions Between The Extracellular Matrix And The Cytoskeleton. *Annual Review of Cell and Developmental Biology*, 4(1), pp.487–525.

Castagnola, E. et al., 2015. Pedot-CNT-coated low-impedance, ultra-flexible, and brain-conformable micro-ECoG arrays. *IEEE Transactions on Neural Systems and Rehabilitation Engineering*, 23(3), pp.342–350.

Cellot, G. et al., 2016. PEDOT:PSS interfaces support the development of neuronal synaptic networks with reduced neuroglia response in vitro. *Frontiers in neuroscience*, 9(521).

Chapman, C.A.R. et al., 2016. Mechanisms of Reduced Astrocyte Surface Coverage in Cortical Neuron-Glia Co-cultures on Nanoporous Gold Surfaces. *Cellular and Molecular*

Bioengineering, 9(3), pp.433–442.

Chapman, C.A.R. et al., 2015. Nanoporous gold as a neural interface coating: Effects of topography, surface chemistry, and feature size. *ACS Applied Materials and Interfaces*, 7(13), pp.7093–7100.

Chen, H. et al., 2011. Multilayered polypyrrole-coated carbon nanotubes to improve functional stability and electrical properties of neural electrodes. *Journal of Physical Chemistry C*, 115(13), pp.5492–5499.

Chen, Z. et al., 2005. Impedance immunosensor based on receptor protein adsorbed directly on porous gold film. *Analytica Chimica Acta*, 553(1-2), pp.190–195.

Chesler, M., 2008. Regulation and Modulation of pH in the Brain. *Brain*, pp.1183–1221.

Cho, S.H. et al., 2008. Biocompatible SU-8-based microprobes for recording neural spike signals from regenerated peripheral nerve fibers. *IEEE Sensors Journal*, 8(11), pp.1830–1836.

Chung, T., Wang, J.Q., Wang, J., et al., 2015. Electrode modifications to lower electrode impedance and improve neural signal recording sensitivity. *Journal of Neural Engineering*, 12(5), p.056018.

Chung, T., Wang, J.Q., Cao, B., et al., 2015. Electrode modifications to lower electrode impedance and improve neural signal recording sensitivity. *Journal of Neural Engineering*, 12(5), p.056018.

Cogan, S.F., 2008. Neural stimulation and recording electrodes. *Annual review of biomedical engineering*, 10, pp.275–309.

Cohen, M. et al., 2004. Spatial and temporal sequence of events in cell adhesion: From molecular recognition to focal adhesion assembly. *ChemBioChem*, 5(10), pp.1393–1399.

Compton, R.G. & Banks, C.E., 2011. *Understanding Voltammetry* 1st ed., Singapore: World Scientific.

Cragg, P., Patterson, L. & Purves, M., 1977. The pH of brain extracellular fluid in the cat. *The Journal of Physiology*, 272(1), p.137.

Cui, X. et al., 2003. In vivo studies of polypyrrole/peptide coated neural probes. *Biomaterials*, 24(5), pp.777–787.

Curtis, A.S.G. et al., 2001. Substratum nanotopography and the adhesion of biological cells. Are symmetry or regularity of nanotopography important? *Biophysical Chemistry*, 94(3), pp.275–283.

Daikhin, L., Kornyshev, a. & Urbakh, M., 1996. Double-layer capacitance on a rough metal surface. *Physical Review E*, 53(6), pp.6192–6199.

Daikhin, L.I., Kornyshev, a. a. & Urbakh, M., 1997. Double layer capacitance on a rough metal surface: Surface roughness measured by “Debye ruler.” *Electrochimica Acta*, 42(19), pp.2853–2860.

Debye, P., 1936. Dielectric properties of pure liquids. *Chemical Reviews*, 19, pp.171–182.

Desai, S.A. et al., 2010. Improving impedance of implantable microwire multi-electrode arrays by ultrasonic electroplating of durable platinum black. *Frontiers in neuroengineering*, 3, p.5.

Devore, J.L., Farnum, N.R. & Doi, J.A., 1999. *Applied Statistics for Engineers and Scientists* 3rd ed. M. Taylor, L. Wheel, & A. Coppola, eds., Stamford: Cengage Learning.

Di, L. et al., 2011. Protein adsorption and peroxidation of rat retinas under stimulation of a neural probe coated with polyaniline. *Acta Biomaterialia*, 7(10), pp.3738–3745.

Diener, A. et al., 2005. Control of focal adhesion dynamics by material surface characteristics. *Biomaterials*, 26(4), pp.383–392.

Doña Rodríguez, J.M., Herrera Melián, J. a. & Pérez Peña, J., 2000. Determination of the Real Surface Area of Pt Electrodes by Hydrogen Adsorption Using Cyclic Voltammetry. *Journal of Chemical Education*, 77(9), p.1195.

Fattahi, P. et al., 2014. A review of organic and inorganic biomaterials for neural interfaces. *Advanced Materials*, 26(12), pp.1846–1885.

Fidler, P.S. et al., 1999. Comparing astrocytic cell lines that are inhibitory or permissive for axon growth: the major axon-inhibitory proteoglycan is NG2. *The Journal of neuroscience : the official journal of the Society for Neuroscience*, 19(20), pp.8778–

8788.

Frackowiak, E. & Beguin, F., 2001. Carbon materials for the electrochemical storage of energy in capacitors. *PERGAMON Carbon*, 39, pp.937–950.

Frantz, C., Stewart, K.M. & Weaver, V.M., 2010. The extracellular matrix at a glance. *Journal of cell science*, 123, pp.4195–4200.

Frumkin, A.N., 1960. The Double Layer in Electrochemistry. *J. Electrochem. Soc*, 107(5), pp.461–472.

García, A.J., 2005. Get a grip: Integrins in cell-biomaterial interactions. *Biomaterials*, 26(36), pp.7525–7529.

García-Gabaldón, M. et al., 2011. Electrochemical study of a simulated spent pickling solution. *International Journal of Electrochemical Science*, 6(2), pp.506–519.

Ghazni, N.F., Cahill, C.M. & Stroman, P.W., 2010. Tactile sensory and pain networks in the human spinal cord and brain stem mapped by means of functional MR imaging. *American Journal of Neuroradiology*, 31(4), pp.661–667.

Hai, A. et al., 2009. Spine-shaped gold protrusions improve the adherence and electrical coupling of neurons with the surface of micro-electronic devices. *Journal of the Royal Society, Interface / the Royal Society*, 6(41), pp.1153–65.

Hamelin, A. & Martins, A.M., 1996. Cyclic voltammetry at gold single-crystal surfaces. Part 2. Behaviour of high-index faces. *Joumal of Electroanalytical Chemistry*, 407, pp.13–21.

Heim, M. et al., 2012. Combined macro-/mesoporous microelectrode arrays for low-noise extracellular recording of neural networks. *Journal of Neurophysiology*, 108(6), pp.1793–1803.

Hu, Z. et al., 2006. Nanopowder molding method for creating implantable high-aspect-ratio electrodes on thin flexible substrates. *Biomaterials*, 27(9), pp.2009–2017.

Johnson, M.D., Otto, K.J. & Kipke, D.R., 2005. Repeated voltage biasing improves unit recordings by reducing resistive tissue impedances. *IEEE Transactions on Neural Systems and Rehabilitation Engineering*, 13(2), pp.160–165.

Kerner, Z., 1998. Impedance of rough capacitive electrodes : the role of surface disorder. ,

448, pp.139–142.

Kerner, Z. & Pajkossy, T., 2000. On the origin of capacitance dispersion of rough electrodes. *Electrochimica Acta*, 46(2-3), pp.207–211.

Kim, S.A., Kim, E.T. & Kim, S.J., 2009. Highly Efficient Cold Sputtered Iridium Oxide Films for Polyimide based Neural Stimulation Electrodes. *Journal of Biomedical Engineering Research*, 30(3), pp.199–204.

Kocherbitov, V., 2015. Surface and Physical Chemistry. , p.Debye Screening Length. Available at: http://www.surfchem.info/calculate/Debye/.

Koklu, A., Sabuncu, A.C. & Beskok, A., 2016. Rough Gold Electrodes for Decreasing Impedance at the Electrolyte/Electrode Interface. *Electrochimica Acta*.

Kolb, D.M. & Schneider, J., 1986. Surface reconstruction in electrochemistry: Au(100-(5 × 20), Au(111)-(1 × 23) and Au(110)-(1 × 2). *Electrochimica Acta*, 31(8), pp.929–936.

Kozai, T.D. et al., 2010. Reduction of neurovascular damage resulting from microelectrode insertion into the cerebral cortex using in vivo two-photon mapping. *J Neural Eng*, 7(4), p.46011.

Kozai, T.D.Y. et al., 2016. Chronic In Vivo Evaluation of PEDOT / CNT for Stable Neural Recordings. *IEEE Trans Biomed Eng*, 63(1), pp.111–119.

Kozai, T.D.Y. et al., 2014. Chronic tissue response to carboxymethyl cellulose based dissolvable insertion needle for ultra-small neural probes. *Biomaterials*, 35(34), pp.9255–9268.

Kozai, T.D.Y., Vazquez, A.L., et al., 2012. In vivo two-photon microscopy reveals immediate microglial reaction to implantation of microelectrode through extension of processes. *Journal of Neural Engineering*, 9(6), p.066001.

Kozai, T.D.Y., Langhals, N.B., et al., 2012. Ultrasmall implantable composite microelectrodes with bioactive surfaces for chronic neural interfaces. *Nature materials*, 11(12), pp.1065–73.

Kurtulus, O. & Seker, E., 2012. Nanotopography Effects on Astrocyte Attachment to Nanoporous Gold Surfaces. In *IEEE EMBS*. pp. 6568–6571.

Lim, J.Y. et al., 2005. Human foetal osteoblastic cell response to polymer-demixed nanotopographic interfaces. *Journal of the Royal Society, Interface / the Royal Society*, 2(2), pp.97–108.

Malaga, K.A. et al., 2016. Data-driven model comparing the effects of glial scarring and tip metallization loss on chronic neural recordings. *Neural Engineering*, 13(1), p.16010.

Martic, S., Rains, M.K. & Kraatz, H.B., 2013. Probing copper/tau protein interactions electrochemically. *Analytical Biochemistry*, 442(2), pp.130–137.

McConnell, G.C. et al., 2009. Implanted neural electrodes cause chronic, local inflammation that is correlated with local neurodegeneration. *Journal of neural engineering*, 6(5), p.056003.

Meijs, S. et al., 2016. Influence of fibrous encapsulation on electro-chemical properties of TiN electrodes. *Medical Engineering and Physics*, 38(5), pp.468–476.

Michel, E., Hernandez, D. & Lee, S.Y., 2016. Electrical conductivity and permittivity maps of brain tissues derived from water content based on T_1 -weighted acquisition. *Magnetic Resonance in Medicine*.

Michel, R. et al., 2008. The Influence of PEG Architecture on Protein Adsorption and Conformation. *Langmuir*, 21(26), pp.12327–12332.

Moulton, S.E. et al., 2003. Investigation of protein adsorption and electrochemical behavior at a gold electrode. *Journal of Colloid and Interface Science*, 261(2), pp.312–319.

Moulton, S.E. et al., 2004. Studies of double layer capacitance and electron transfer at a gold electrode exposed to protein solutions. *Electrochimica Acta*, 49(24), pp.4223–4230.

Negi, S. et al., 2010. In vitro comparison of sputtered iridium oxide and platinum-coated neural implantable microelectrode arrays. *Biomed. Mater*, 5, pp.15007–9.

Newbold, C. et al., 2010. Changes in biphasic electrode impedance with protein adsorption and cell growth. *Journal of neural engineering*, 7(5), p.056011.

Ngoka, L.C., 2008. Sample prep for proteomics of breast cancer: proteomics and gene ontology reveal dramatic differences in protein solubilization preferences of

radioimmunoprecipitation assay and urea lysis buffers. *Proteome science*, 6, p.30.

Oehrlein, G.S. & Kurogi, Y., 1998. Sidewall surface chemistry in directional etching processes. *Materials Science and Engineering: R: Reports*, 24(4), pp.153–183.

Oehrlein, G.S. & Lee, Y.H., 1987. Reactive ion etching related Si surface residues and subsurface damage: Their relationship to fundamental etching mechanisms. *Journal of Vacuum Science & Technology A: Vacuum, Surfaces, and Films*, 5(4), p.1585.

Ohno, Y. et al., 2009. Electrolyte-Gated Graphene Field-Effect Transistors for Detecting pH and Protein Adsorption. *American Chemical Society*, 9(9), pp.2–6.

Oldham, K.B., 1981. Edge effects in semiinfinite diffusion. *Journal of Electroanalytical Chemistry*, 122(C), pp.1–17.

Oldham, K.B. & Zoski, C.G., 1988. Comparison of voltammetric steady states at hemispherical and disc microelectrodes. *Journal of Electroanalytical Chemistry*, 256(1), pp.11–19.

Otto, K.J., Johnson, M.D. & Kipke, D.R., 2006. Voltage pulses change neural interface properties and improve unit recordings with chronically implanted microelectrodes. *IEEE Transactions on Biomedical Engineering*, 53(2), pp.333–340.

Pajkossy, T., 1997. Capacitance dispersion on solid electrodes: anion adsorption studies on gold single crystal electrodes. *Solid State Ionics*, 94(1-4), pp.123–129.

Pajkossy, T., 1991. Electrochemistry at fractal surfaces. *Journal of Electroanalytical Chemistry*, 300(1-2), pp.1–11.

Pajkossy, T., 2005. Impedance spectroscopy at interfaces of metals and aqueous solutions - Surface roughness, CPE and related issues. *Solid State Ionics*, 176(25-28), pp.1997–2003.

Park, J.H. et al., 2003. The correlation of the complex dielectric constant and blood glucose at low frequency. *Biosensors and Bioelectronics*, 19(4), pp.321–324.

Park, J.M. et al., 1992. Effects of protein charge heterogeneity in protein-polyelectrolyte complexation. *Macromolecules*, 25(1), pp.290–295.

Patel, J. et al., 2013. Electrochemical properties of nanostructured porous gold electrodes in

biofouling solutions. *Analytical Chemistry*, 85(23), pp.11610–11618.

Patel, P.R. et al., 2015. Insertion of linear 8.4 *μ* m diameter 16 channel carbon fiber electrode arrays for single unit recordings. *Journal of Neural Engineering*, 12(4), p.046009.

a Powell, E.M. et al., 1997. Mechanisms of astrocyte-directed neurite guidance. *Cell and Tissue Research*, 290(2), pp.385–393.

b Powell, E.M., Fawcett, J.W. & Geller, H.M., 1997. Proteoglycans provide neurite guidance at an astrocyte boundary. *Molecular and cellular neurosciences*, 10(1-2), pp.27–42.

Prasad, A. et al., 2012. Comprehensive characterization and failure modes of tungsten microwire arrays in chronic neural implants. *J. Neural Eng. J. Neural Eng*, 9(9).

Roitbak, T. & Syková, E., 1999. Diffusion barriers evoked in the rat cortex by reactive astrogliosis. *GLIA*, 28(1), pp.40–48.

Rushworth, J. V. et al., 2014. A label-free electrical impedimetric biosensor for the specific detection of Alzheimer's amyloid-beta oligomers. *Biosensors and Bioelectronics*, 56, pp.83–90.

Sakurai-Yamashita, Y. et al., 2006. Expression of MCP-1 in the hippocampus of SHRSP with ischemia-related delayed neuronal death. *Cellular and Molecular Neurobiology*, 26(4-6), pp.823–831.

Salakhutdinov, I. et al., 2008. Fibronectin adsorption to nanopatterned silicon surfaces. *Journal of Nanomaterials*, 2008(1).

Schaefer, L. & Schaefer, R.M., 2010. Proteoglycans: From structural compounds to signaling molecules. *Cell and Tissue Research*, 339(1), pp.237–246.

Seker, E. et al., 2012. Microfabrication-compatible nanoporous gold foams as biomaterials for drug delivery. *Advanced Healthcare Materials*, 1(2), pp.172–176.

Seker, E. et al., 2010. The fabrication of low-impedance nanoporous gold multiple-electrode arrays for neural electrophysiology studies. *Nanotechnology*, 21(12), p.125504.

Selhuber-Unkel, C. et al., 2008. Cooperativity in Adhesion Cluster Formation during Initial Cell Adhesion. *Biophysical Journal*, 95(11), pp.5424–5431.

Smith-Thomas, L.C. et al., 1995. Increased axon regeneration in astrocytes grown in the presence of proteoglycan synthesis inhibitors. *Journal of cell science*, 108 (Pt 3, pp.1307–1315.

Sommakia, S. et al., 2014. Resistive and reactive changes to the impedance of intracortical microelectrodes can be mitigated with polyethylene glycol under acute in vitro and in vivo settings. *Frontiers in neuroengineering*, 7(August), p.33.

Sommakia, S., Rickus, J.L. & Otto, K.J., 2009. Effects of adsorbed proteins, an antifouling agent and long-duration DC voltage pulses on the impedance of silicon-based neural microelectrodes. In *Proceedings of the 31st Annual International Conference of the IEEE Engineering in Medicine and Biology Society: Engineering the Future of Biomedicine, EMBC 2009*. pp. 7139–7142.

Szarowski, D.H. et al., 2003. Brain responses to micro-machined silicon devices. *Brain Research*, 983(1-2), pp.23–35.

Thomas, G.M., 2012. Does Controlled Roughening of a Surface Increase Its Capacitance ?

Tian, Z.Q., Ren, B. & Wu, D.Y., 2002. Surface-enhanced Raman scattering: From noble to transition metals and from rough surfaces to ordered nanostructures. *Journal of Physical Chemistry B*, 106(37), pp.9463–9483.

Triplett, J.W. & Pavalko, F.M., 2006. Disruption of alpha-actinin-integrin interactions at focal adhesions renders osteoblasts susceptible to apoptosis. *American journal of physiology. Cell physiology*, 291(5), pp.C909–21.

Tura, A. et al., 2007. Impedance spectroscopy of solutions at physiological glucose concentrations. *Biophysical Chemistry*, 129(2-3), pp.235–241.

Vahidpour, F. et al., 2016. All-diamond functional surface micro-electrode arrays for brain-slice neural analysis. *Physica Status Solidi (a)*, 8, pp.1–8.

Venkatraman, S. et al., 2009. PEDOT coated microelectrode arrays for chronic neural recording and stimulation. *2009 4th International IEEE/EMBS Conference on Neural Engineering, NER '09*, 4, pp.383–386.

Volterra, A. & Meldolesi, J., 2009. Astroctes, from brain glue to communication elements:

The revelution continues. *Dialogues in Clinical Neuroscience*, 11(3), pp.281–296.

Walsh, E. et al., 1992. Neuronal survival and neurite extension supported by astrocytes co-cultured in transwells. *Neuroscience Letters*, 138(1), pp.103–106.

Ward, M.D. & Hammer, D.A., 1993. A theoretical analysis for the effect of focal contact formation on cell-substrate attachment strength. *Biophysical Journal*, 64(3), pp.936–959.

Westergren-Thorsson, G. et al., 1998. Differential expressions of mRNA for proteoglycans, collagens and transforming growth factor-?? in the human cervix during pregnancy and involution. *Biochimica et Biophysica Acta - Molecular Basis of Disease*, 1406(2), pp.203–213.

Wight, T.N., 2002. Versican: A versatile extracellular matrix proteoglycan in cell biology. *Current Opinion in Cell Biology*, 14(5), pp.617–623.

Williams, D.F., Askill, I.N. & Smith, R., 1985. Protein absorption and desorption phenomena on clean metal surfaces. *Journal of biomedical materials research*, 19, pp.313–320.

Xue, P. et al., 2014. Protein covalently conjugated SU-8 surface for the enhancement of mesenchymal stem cell adhesion and proliferation. *Langmuir*, 30(11), pp.3110–3117.

Ying, P. et al., 2004. Adsorption of human serum albumin onto gold: A combined electrochemical and ellipsometric study. *Journal of Colloid and Interface Science*, 279(1), pp.95–99.

Zaidi, K.F. et al., 2010. In vitro Models for Measuring Charge Storage Capacity. *IFMBE Proceedings*, 32, pp.97–100.

Zhang, H. et al., 2012. Layered nanocomposites from gold nanoparticles for neural prosthetic devices. *Nano Letters*, 12(7), pp.3391–3398.

Zhang, J. et al., 2012. Label-Free Electrochemical Detection of Tetracycline by an Aptamer Nano-Biosensor. *Analytical Letters*, 45(9), pp.986–992.

Zhao, H. et al., 1999. Surface-roughness effect on capacitance and leakage current of an insulating film.

Zheng, Y. et al., 2013. Electrical measurement of red blood cell deformability on a

microfluidic device. *Lab on a chip*, 13(16), pp.3275–83.